Dear Author,

Here are the proofs of your article.

- You can submit your corrections **online**, via **e-mail** or by **fax**.
- For **online** submission please insert your corrections in the online correction form. Always indicate the line number to which the correction refers.
- You can also insert your corrections in the proof PDF and **email** the annotated PDF.
- For fax submission, please ensure that your corrections are clearly legible. Use a fine black pen and write the correction in the margin, not too close to the edge of the page.
- Remember to note the **journal title**, **article number**, and **your name** when sending your response via e-mail or fax.
- **Check** the metadata sheet to make sure that the header information, especially author names and the corresponding affiliations are correctly shown.
- **Check** the questions that may have arisen during copy editing and insert your answers/ corrections.
- **Check** that the text is complete and that all figures, tables and their legends are included. Also check the accuracy of special characters, equations, and electronic supplementary material if applicable. If necessary refer to the *Edited manuscript*.
- The publication of inaccurate data such as dosages and units can have serious consequences. Please take particular care that all such details are correct.
- Please **do not** make changes that involve only matters of style. We have generally introduced forms that follow the journal's style.
  Substantial changes in content, e.g., new results, corrected values, title and authorship are not allowed without the approval of the responsible editor. In such a case, please contact the Editorial Office and return his/her consent together with the proof.
- If we do not receive your corrections **within 48 hours**, we will send you a reminder.
- Your article will be published **Online First** approximately one week after receipt of your corrected proofs. This is the **official first publication** citable with the DOI. **Further changes are, therefore, not possible.**
- The **printed version** will follow in a forthcoming issue.

Please note

After online publication, subscribers (personal/institutional) to this journal will have access to the complete article via the DOI using the URL: http://dx.doi.org/[DOI].
If you would like to know when your article has been published online, take advantage of our free alert service. For registration and further information go to: http://www.link.springer.com.

Due to the electronic nature of the procedure, the manuscript and the original figures will only be returned to you on special request. When you return your corrections, please inform us if you would like to have these documents returned.

Metadata of the article that will be visualized in OnlineFirst

ArticleTitle	Bounds on size effects in composites via homogenization accounting for general interfaces	
Article Sub-Title		
Article CopyRight	Springer-Verlag GmbH Germany, part of Springer Nature (This will be the copyright line in the final PDF)	
Journal Name	Continuum Mechanics and Thermodynamics	
Corresponding Author	Family Name	**Javili**
	Particle	
	Given Name	**Ali**
	Suffix	
	Division	Department of Mechanical Engineering
	Organization	Bilkent University
	Address	06800, Ankara, Turkey
	Phone	
	Fax	
	Email	ajavili@bilkent.edu.tr
	URL	
	ORCID	http://orcid.org/0000-0001-7965-7088
Author	Family Name	**Firooz**
	Particle	
	Given Name	**Soheil**
	Suffix	
	Division	Department of Mechanical Engineering
	Organization	Bilkent University
	Address	06800, Ankara, Turkey
	Phone	
	Fax	
	Email	soheil.firooz@bilkent.edu.tr
	URL	
	ORCID	
Author	Family Name	**Chatzigeorgiou**
	Particle	
	Given Name	**George**
	Suffix	
	Division	
	Organization	LEM3-UMR 7239 CNRS, Arts et Metiers ParisTech Metz
	Address	4 Rue Augustin Fresnel, 57078, Metz, France
	Phone	
	Fax	
	Email	georges.chatzigeorgiou@ensam.eu
	URL	

	ORCID	
Author	Family Name	**Meraghni**
	Particle	
	Given Name	**Fodil**
	Suffix	
	Division	
	Organization	LEM3-UMR 7239 CNRS, Arts et Metiers ParisTech Metz
	Address	4 Rue Augustin Fresnel, 57078, Metz, France
	Phone	
	Fax	
	Email	fodil.meraghni@ensam.eu
	URL	
	ORCID	

Schedule	Received	18 December 2018
	Revised	
	Accepted	25 May 2019

Abstract	This manuscript provides novel bounds and estimates, for the first time, on size-dependent properties of composites accounting for generalized interfaces in their microstructure, via analytical homogenization verified by computational analysis. We extend both the composite cylinder assemblage and Mori–Tanaka approaches to account for the general interface model. Our proposed strategy does not only determine the overall response of composites, but also it provides information about the local fields for each phase of the medium including the interface. We present a comprehensive study on a broad range of interface parameters, stiffness ratios and sizes. Our analytical solutions are in excellent agreement with the computational results using the finite element method. Based on the observations throughout our investigations, two notions of *size-dependent bounds* and *ultimate bounds* on the effective response of composites are introduced which yield a significant insight into the size effects, particularly important for the design of nano-composites.

Keywords (separated by '-')	General interface - Size effects - Ultimate bounds - Size-dependent bounds - Homogenization - Composites
Footnote Information	Communicated by Andreas Öchsner.

Continuum Mech. Thermodyn.
https://doi.org/10.1007/s00161-019-00796-w

ORIGINAL ARTICLE

Soheil Firooz · George Chatzigeorgiou · Fodil Meraghni · Ali Javili

Bounds on size effects in composites via homogenization accounting for general interfaces

Received: 18 December 2018 / Accepted: 25 May 2019

Abstract This manuscript provides novel bounds and estimates, for the first time, on size-dependent properties of composites accounting for generalized interfaces in their microstructure, via analytical homogenization verified by computational analysis. We extend both the composite cylinder assemblage and Mori–Tanaka approaches to account for the general interface model. Our proposed strategy does not only determine the overall response of composites, but also it provides information about the local fields for each phase of the medium including the interface. We present a comprehensive study on a broad range of interface parameters, stiffness ratios and sizes. Our analytical solutions are in excellent agreement with the computational results using the finite element method. Based on the observations throughout our investigations, two notions of *size-dependent bounds* and *ultimate bounds* on the effective response of composites are introduced which yield a significant insight into the size effects, particularly important for the design of nano-composites.

Keywords General interface · Size effects · Ultimate bounds · Size-dependent bounds · Homogenization · Composites

1 Introduction

Interphases between the constituents of heterogeneous materials play a crucial role on the overall material response and particularly at small scales, due to the large area-to-volume ratio. A common strategy to model the interphases is to replace them by a zero-thickness general interface [1] characterized by displacement and traction jumps. This idea was initially proposed by Sanchez-Palencia et al. [2,3] and followed by Hashin [4] for a thermal problem. Since the area-to-volume ratio is proportional to the inverse of the dimension, accounting for interfaces in homogenization results in size-dependent properties hence, capturing the size effects, unlike the classical homogenization [5–7] that lacks a length scale. In this contribution, we present two analytical

Communicated by Andreas Öchsner.

S. Firooz · A. Javili (✉)
Department of Mechanical Engineering, Bilkent University, 06800 Ankara, Turkey
E-mail: ajavili@bilkent.edu.tr

S. Firooz
E-mail: soheil.firooz@bilkent.edu.tr

G. Chatzigeorgiou · F. Meraghni
LEM3-UMR 7239 CNRS, Arts et Metiers ParisTech Metz, 4 Rue Augustin Fresnel, 57078 Metz, France
E-mail: georges.chatzigeorgiou@ensam.eu

F. Meraghni
E-mail: fodil.meraghni@ensam.eu

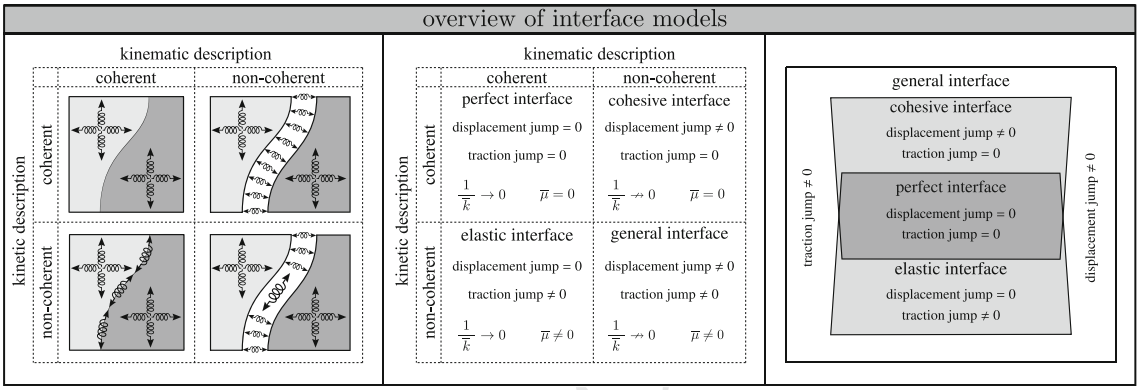

Fig. 1 Categorization of the interface models based on their kinetic or kinematic behavior. The perfect interface model does not allow for the displacement jump nor traction jump. The cohesive interface model has continuous traction field, whereas the displacement jump is allowed across the interface. In the elastic interface model, the displacement jump across the interface is zero, whereas the traction jump is permissible. All the models are unified in the general interface model in which both the displacement jump and traction jump across the interface are possible. Two interface properties of $\overline{\mu}$ and $\overline{k}$ characterize the interface behavior. The interface stiffness against opening is denoted $\overline{k}$, and the interface resistance against stretch is denoted $\overline{\mu}$

solutions to determine the overall behavior of composites via a homogenization framework accounting for generalized interfaces. In addition, computational analysis is carried out to evaluate the performance of the analytical solutions.

Figure 1 categorizes the interface models based on their kinetic (tractions) and kinematic (displacements) features. The interface is referred to as perfect if the traction and displacement fields are continuous across the interface, and thus, the perfect interface model is coherent both kinetically and kinematically.

The elastic interface model is kinematically coherent but kinetically non-coherent and hence semi-perfect. The main assumption of the interface elasticity theory [8–15] is that the interface is allowed to have its own thermodynamic structure. This assumption could result in a traction jump across the interface due to the Young–Laplace equation [16–18]. The subject of surface and interface elasticity has been extensively studied in [19–35] among others. The cohesive interface model allows for the displacement jump but not for the traction jump. This model is kinetically coherent and kinematically non-coherent. The cohesive interface model emerges in a variety of studies dating from the seminal works [36–38] to its extensions and applications in [39–57]. The general interface model is a unified version of all the aforementioned interface models where both the displacement jump and traction jump are admissible. The general interface has been examined in a fundamental contribution by Hashin [58] and further studied in [59–68] among others.

In the past decade, scale-dependent macroscopic behavior due to the microscale elasticity has been comprehensively studied from both analytical [69–79] and computational [80–84] perspectives. Comparisons with atomistic simulations and experiments in [85–90] justify that the size effects due to interfaces are physically meaningful. The underlying assumption in this contribution is that the size effects are only observed due to the presence of the interface at the microstructure. While the surface/interface elasticity itself may be explained by the tangential contributions of second-gradient continua on the boundary, the full contributions of second-gradient continua in the bulk are not taken into account. Obviously, one must eventually develop a complete model in which both strain-gradient and surface/interface elasticity are present. Only then, one can claim whether or not the size effect due to the interface is correlated with those associated with the strain-gradient effects. See [23] for an excellent study on size-dependent effects in nano-materials.

The term "size" in this contribution refers to the physical size of a microstructure. Figure 2 illustrates schematically the definition of the size. The volume fraction of the inclusion is denoted f. For a given volume fraction and size, the radii of the inclusion and the matrix can be calculated. Throughout this manuscript, the macroscopic quantities are distinct from their microscopic counterparts by a left superscript "M." For instance, ${}^{\mathrm{M}}\{\bullet\}$ is a macroscopic quantity with its counterpart being $\{\bullet\}$ at the microscale. Interface quantities are distinguished from the bulk quantities by a bar placed on top them. That is, $\{\overline{\bullet}\}$ denotes an interface quantity with its bulk counterpart $\{\bullet\}$. Moreover, the average and the jump operators across the interface are denoted by $\{\!\{\{\bullet\}\}\!\}$ and $[\![\{\bullet\}]\!]$, respectively.

The rest of this manuscript is organized as follows. Section 2 elaborates on the problem definition and provides the governing equations. In Sect. 3, the analytical approaches accounting for the general interface

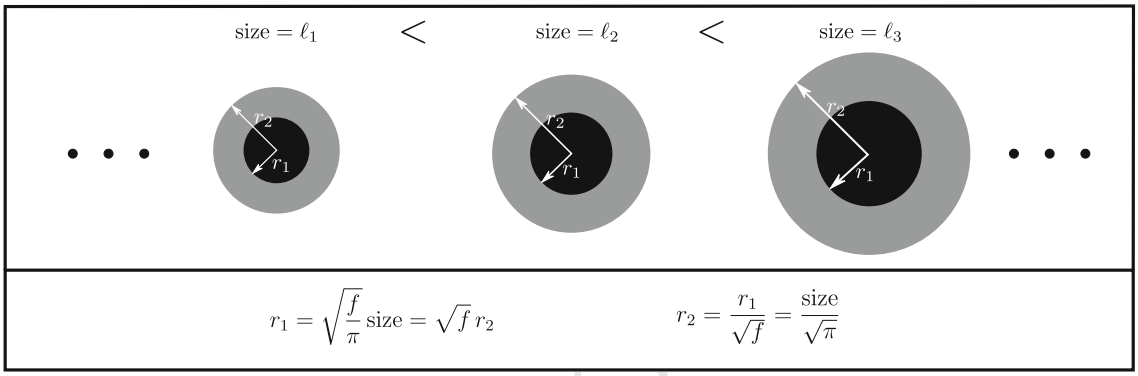

Fig. 2 Illustration of the term "size." Having the volume fraction, the radius of the inclusion and the matrix can be obtained for each specific size. As a result, size is proportional to the radius of the inclusion or that of the matrix

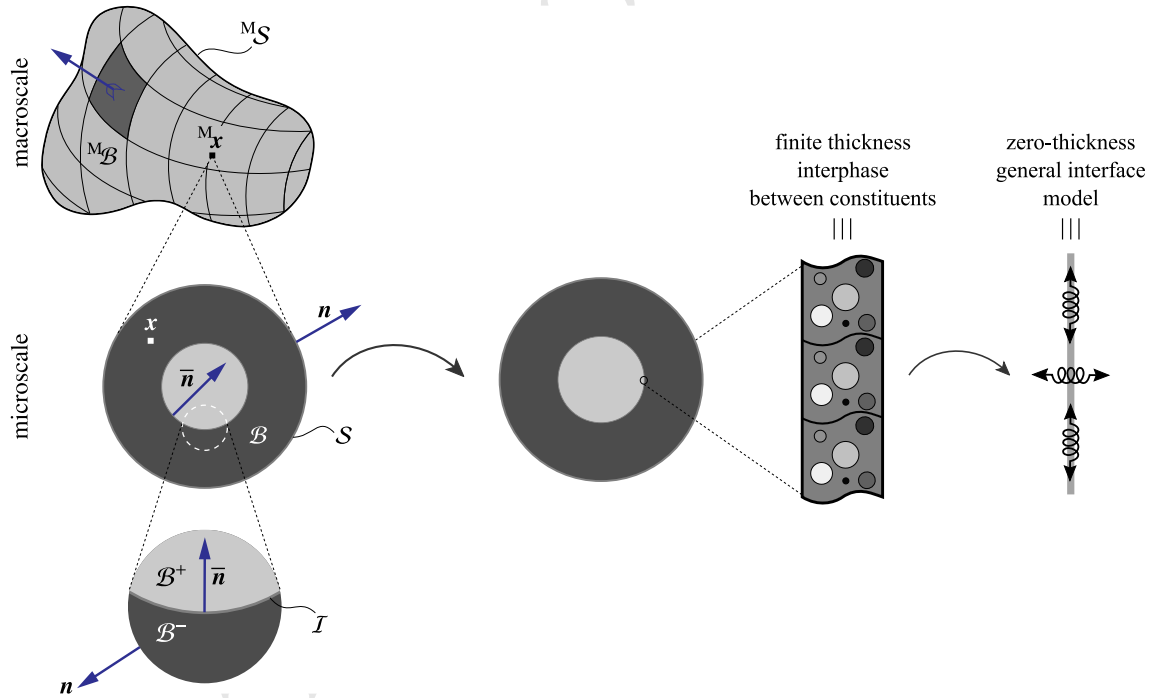

Fig. 3 Problem definition for homogenization including the general interface model. The macrostructure is shown as well as the microstructure which is in fact the RVE. It is assumed that the constitutive laws at the microscale are known and by prescribing a macroscopic strain ${}^{\mathrm{M}}\boldsymbol{\varepsilon}$ on the microstructure, the macroscopic stress ${}^{\mathrm{M}}\boldsymbol{\sigma}$ is obtained via averaging. A finite-thickness interphase is replaced with a zero-thickness interface model. The classical interface models cannot capture heterogeneous material layer, and thus, the general interface model is required

model are presented. Numerical examples are provided in Sect. 4 to compare the computational and analytical results. Section 5 concludes this work and provides further outlook for future contributions.

2 Governing equations

In this section, the governing equations of continua embedding a general interface are given. For the sake of brevity, only the final form of the essential equations are stated. For more details on the derivations, the reader is referred to [1,65,91]. Consider a continuum body taking the configuration ${}^{\mathrm{M}}\mathcal{B}$ at the macroscale, as shown in Fig. 3, with its corresponding RVE at the microscale denoted as $\mathcal{B}$. A general interface model is required to replace the finite-thickness interphase between the constituents [92]. It is assumed that the constitutive behavior of the material at the microscale is known and the macroscopic overall response of the medium is obtained

via averaging over the RVE [see [93–98], among others]. In doing so, a macroscopic strain ${}^{\mathrm{M}}\boldsymbol{\varepsilon}$ is prescribed on the microstructure and the macroscopic stress ${}^{\mathrm{M}}\boldsymbol{\sigma}$ is obtained. Moreover, to establish a computational homogenization framework, an appropriate RVE must be chosen such that (i) it is small enough to guarantee scale separation and (ii) it is large enough to be representative of the microstructure. For more details on the definition of RVE, see [99–102]. Here, we significantly simplify the RVE to a circular microstructure in order to obtain in-plane isotropic effective behavior of the RVE suitable for comparison with the proposed analytical estimates.

The interface $\mathcal{I}$ separates the microstructure into two subdomains $\mathcal{B}^+$ and $\mathcal{B}^-$. The outward unit normal to the external boundary is denoted as $\boldsymbol{n}$, whereas $\overline{\boldsymbol{n}}$ defines the interface unit normal vector pointing from the minus side of the interface to its plus side. The displacement field is denoted as $\boldsymbol{u}$, and the interface displacement $\overline{\boldsymbol{u}}$ is defined by the average displacement across the interface conforming to the definition of the mid-surface. The displacement average and the displacement jump across the interface read

$$\overline{\boldsymbol{u}} := \{\!\{\boldsymbol{u}\}\!\} = \frac{1}{2}\left[\boldsymbol{u}^+ + \boldsymbol{u}^-\right] \quad \text{and} \quad [\![\boldsymbol{u}]\!] = \left[\boldsymbol{u}^+ - \boldsymbol{u}^-\right], \tag{1}$$

respectively, where $\boldsymbol{u}^+$ is the displacement of the plus side of the interface and $\boldsymbol{u}^-$ is the displacement of the minus side of the interface. The strain field in the bulk and on the interface read

$$\boldsymbol{\varepsilon} = \frac{1}{2}\left[\boldsymbol{i}\cdot\operatorname{grad}\boldsymbol{u} + \left[\operatorname{grad}\boldsymbol{u}\right]^{\mathrm{t}}\cdot\boldsymbol{i}\right] \quad \text{in } \mathcal{B} \quad \text{and} \quad \overline{\boldsymbol{\varepsilon}} = \frac{1}{2}\left[\overline{\boldsymbol{i}}\cdot\overline{\operatorname{grad}}\,\overline{\boldsymbol{u}} + \left[\overline{\operatorname{grad}}\,\overline{\boldsymbol{u}}\right]^{\mathrm{t}}\cdot\overline{\boldsymbol{i}}\right] \quad \text{on } \mathcal{I}, \tag{2}$$

where $\boldsymbol{i}$ is the identity tensor. The operator $\overline{\operatorname{grad}}\{\bullet\}$ characterizes the projection of the gradient onto the interface as $\overline{\operatorname{grad}}\{\bullet\} = \operatorname{grad}\{\bullet\}\cdot\overline{\boldsymbol{i}}$ with $\overline{\boldsymbol{i}} = \boldsymbol{i} - \overline{\boldsymbol{n}}\otimes\overline{\boldsymbol{n}}$. Note the contraction $\overline{\boldsymbol{i}}\cdot\overline{\operatorname{grad}}\,\overline{\boldsymbol{u}}$ enforces the projection of the interface displacement gradient onto the interface.

The total energy density of the medium consists of the bulk free energy density ψ and the interface free energy density $\overline{\psi}$. The bulk free energy density is assumed to be only a function of the strain field $\psi = \psi(\boldsymbol{\varepsilon})$. The interface free energy density is assumed to be a function of both interface strain and interface displacement jump as $\overline{\psi} = \overline{\psi}(\overline{\boldsymbol{\varepsilon}}, [\![\boldsymbol{u}]\!])$. That is, the contributions of higher gradients of the interface strain or interface curvature are not taken into account. Connecting the bulk and interface energy densities to their microscale energy conjugates, the constitutive equations read

$$\boldsymbol{\sigma} = \frac{\partial\psi}{\partial\boldsymbol{\varepsilon}} \quad \text{in } \mathcal{B}, \qquad \overline{\boldsymbol{\sigma}} = \frac{\partial\overline{\psi}}{\partial\overline{\boldsymbol{\varepsilon}}} \quad \text{and} \quad \overline{\boldsymbol{t}} = \frac{\partial\overline{\psi}}{\partial[\![\boldsymbol{u}]\!]} \quad \text{on } \mathcal{I}, \tag{3}$$

where $\overline{\boldsymbol{t}}$ is the interface traction as $\overline{\boldsymbol{t}} := \{\!\{\boldsymbol{\sigma}\}\!\}\cdot\overline{\boldsymbol{n}}$. The balance equations in the absence of external forces read

$$\begin{aligned} &\operatorname{div}\boldsymbol{\sigma} = \boldsymbol{0} \quad \text{in } \mathcal{B}, && \boldsymbol{\sigma}\cdot\boldsymbol{n} = \boldsymbol{t} \quad \text{on } \mathcal{S}, \\ &\overline{\operatorname{div}}\,\overline{\boldsymbol{\sigma}} + [\![\boldsymbol{\sigma}]\!]\cdot\overline{\boldsymbol{n}} = \boldsymbol{0} \quad \text{on } \mathcal{I} \text{ (along the interface)}, && \{\!\{\boldsymbol{\sigma}\}\!\}\cdot\overline{\boldsymbol{n}} = \overline{\boldsymbol{t}} \quad \text{on } \mathcal{I} \text{ (across the interface)}, \end{aligned} \tag{4}$$

with $\boldsymbol{t}$ being the traction on the boundary $\mathcal{S}$. The interface divergence operator $\overline{\operatorname{div}}\{\bullet\} = \operatorname{grad}\{\bullet\} : \overline{\boldsymbol{i}}$ embeds the interface curvature operator. The constitutive material behavior for the bulk and interface reads

$$\boldsymbol{\sigma} = 2\,\mu\,\boldsymbol{\varepsilon} + \lambda\,[\boldsymbol{\varepsilon} : \boldsymbol{i}]\,\boldsymbol{i} \quad \text{in } \mathcal{B}, \qquad \overline{\boldsymbol{\sigma}} = 2\,\overline{\mu}\,\overline{\boldsymbol{\varepsilon}} + \overline{\lambda}\left[\overline{\boldsymbol{\varepsilon}} : \overline{\boldsymbol{i}}\right]\overline{\boldsymbol{i}} \quad \text{and} \quad \overline{\boldsymbol{t}} = \overline{k}\,[\![\boldsymbol{u}]\!] \quad \text{on } \mathcal{I}, \tag{5}$$

in which λ and μ are the bulk Lamé parameters and $\overline{\lambda}$ and $\overline{\mu}$ are the interface Lamé parameters. The interface Lamé parameters correspond to the interface in-plane resistance against stretches. The interface orthogonal resistance, $\overline{k}$, represents the interface resistance against opening. Without loss of generality, it can be shown that for the two-dimensional setting here $\overline{\lambda} = 0$ can be assumed since the resistance along an isotropic interface can be sufficiently captured with only one interface parameter.

Next, we briefly elaborate on the micro- to macro-transition. The macroscopic strain and stress can be obtained through boundary integrals of the microscopic quantities as

$${}^{\mathrm{M}}\boldsymbol{\varepsilon} = \frac{1}{\mathscr{V}}\int_{\mathcal{S}}\frac{1}{2}\left[\boldsymbol{u}\otimes\boldsymbol{n} + \boldsymbol{n}\otimes\boldsymbol{u}\right]\mathrm{d}A, \qquad {}^{\mathrm{M}}\boldsymbol{\sigma} = \frac{1}{\mathscr{V}}\int_{\mathcal{S}}\boldsymbol{t}\otimes\boldsymbol{x}\,\mathrm{d}A. \tag{6}$$

Exploiting the divergence theorem, the above relations simplify to the averages

$${}^{\mathrm{M}}\boldsymbol{\varepsilon} = \frac{1}{\mathscr{V}}\int_{\mathcal{B}}\boldsymbol{\varepsilon}\,\mathrm{d}V + \frac{1}{\mathscr{V}}\int_{\mathcal{I}}\frac{1}{2}\left[[\![\boldsymbol{u}]\!]\otimes\overline{\boldsymbol{n}} + \overline{\boldsymbol{n}}\otimes[\![\boldsymbol{u}]\!]\right]\mathrm{d}A, \qquad {}^{\mathrm{M}}\boldsymbol{\sigma} = \frac{1}{\mathscr{V}}\int_{\mathcal{B}}\boldsymbol{\sigma}\,\mathrm{d}V + \frac{1}{\mathscr{V}}\int_{\mathcal{I}}\overline{\boldsymbol{\sigma}}\,\mathrm{d}A. \tag{7}$$

Table 1 The relations between the interface and bulk properties for transversely isotropic composites in terms of the material parameters in Sect. 2 and the commonly accepted notation in analytical homogenization employed in Sect. 3. The parameters in the first row correspond to a generic case but in the second row correspond to a more specific (transversely isotropic) case of interest here

Bulk					Interface						
μ_{ax}	μ_{tr}	κ_{tr}	l	n	$\overline{\mu}_{\mathrm{ax}}$	$\overline{m}$	$\overline{n}$	$\overline{l}$	$\overline{k}_r$	$\overline{k}_\theta$	$\overline{k}_z$
μ	μ	$\lambda+\mu$	λ	$\lambda+2\mu$	$\overline{\mu}$	$2\overline{\mu}$	$2\overline{\mu}$	0	$\overline{k}$	$\overline{k}$	$\overline{k}$

μ_{ax} : axial shear modulus
μ_{tr} : transverse shear modulus
κ_{tr} : transverse bulk modulus
l : stiffness in rz and θz directions
n : axial stiffness
μ : shear modulus
λ : first Lamé parameter

$\overline{\mu}_{\mathrm{ax}}$: interface axial shear modulus
$\overline{m}$: interface transverse shear parameter
$\overline{n}$: interface axial stiffness
$\overline{l}$: interface stiffness in θz direction
$\overline{k}_r$: interface orthogonal resistance in r
$\overline{k}_\theta$: interface orthogonal resistance in θ
$\overline{k}_z$: interface orthogonal resistance in z
$\overline{\mu}$: interface in-plane resistance
$\overline{k}$: interface orthogonal resistance

Finally, the Hill–Mandel condition must be employed to guarantee the energy equivalence between the two scales. The interface enhanced Hill–Mandel condition reads

$$\delta^{\mathrm{M}}\psi \overset{!}{=} \frac{1}{\mathscr{V}}\int_{\mathcal{B}} \delta\psi \,\mathrm{d}V + \frac{1}{\mathscr{V}}\int_{\mathcal{I}} \delta\overline{\psi}\,\mathrm{d}A\,, \tag{8}$$

where $\overset{!}{=}$ shows the conditional equality. Utilizing the Hill's lemma, after some steps the Hill–Mandel condition (8) simplifies to the boundary integral

$$\int_{\mathcal{S}} \left[\delta\boldsymbol{u} - \delta^{\mathrm{M}}\boldsymbol{\varepsilon}\cdot\boldsymbol{x}\right]\cdot\left[\boldsymbol{t} - {}^{\mathrm{M}}\boldsymbol{\sigma}\cdot\boldsymbol{n}\right]\mathrm{d}A \overset{!}{=} 0\,, \tag{9}$$

identifying appropriate boundary conditions on the RVE. Among various boundary conditions satisfying the Hill–Mandel condition, the canonical ones of interest here are the linear displacement boundary condition (DBC) and constant traction boundary condition (TBC). See Firooz et al. [103] for a comprehensive study on the influences of the boundary condition as well as the RVE type on the overall behavior of composites.

3 Analytical estimates

The aim of this section is to elaborate the analytical methods to determine the overall behavior of fiber composites embedding general interfaces. First, the preliminaries of the RVE problem for fiber reinforced composites is provided. Second, we extend the composite cylinder assemblage approach and the generalized self-consistent method to account for general interfaces resulting in bounds and estimates on the macroscopic properties of composites. Finally, an interface enhanced Mori–Tanaka method is developed to incorporate general interfaces which not only provides the overall properties but also determines the state of the stress and strain in each phase of the medium including the interface. Table 1 gathers the relations between the material parameters in Sect. 2 and the commonly accepted notation in analytical homogenization employed in this section as well as the physical meaning of each modulus.

In passing, we shall add that the composite cylinders assemblage (CCA) framework has been designed to account for transversely isotropic constituents at most. Further anisotropy does not allow to identify analytical solutions in boundary value problems like those presented in this manuscript; at least this cannot be done in a straightforward manner. Cylindrical orthotropy of the fiber and the interface, however, has been addressed for similar type of boundary value problems in [104]. To the best of the authors knowledge, no further anisotropy has been studied so far using the composite cylinders assemblage approach. Considering Eshelby-based mean-field approaches, one could follow a strategy similar to the one described by Dinzart and Sabar [105] for general anisotropy of the constituents.

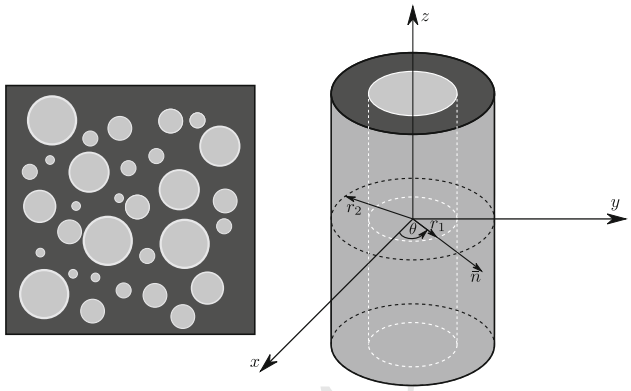

Fig. 4 Heterogeneous medium and its corresponding appropriate RVE considered in our problem. The inner radius shows the radius of the fiber, whereas the outer one shows the radius of the matrix. The interface lies at $r = r_1$

3.1 Preliminaries of the RVE problem for fiber composites

Figure 4 demonstrates the heterogeneous medium and its underlying RVE consisting of two concentric cylinders corresponding to the fiber (phase 1) and matrix (phase 2) with the interface lying at $r = r_1$. The volume fraction of the fiber is $f = {r_1}^2/{r_2}^2$. Obviously, for the problem of interest here, it is more convenient to express the equilibrium equations and the constitutive law in cylindrical coordinate system with coordinates r, θ and z.

For transversely isotropic materials, the constitutive material behavior in Voigt notation reads

$$\begin{bmatrix} \sigma_{rr} \\ \sigma_{\theta\theta} \\ \sigma_{zz} \\ \sigma_{r\theta} \\ \sigma_{rz} \\ \sigma_{\theta z} \end{bmatrix} = \begin{bmatrix} \kappa_{\text{tr}} + \mu_{\text{tr}} & \kappa_{\text{tr}} - \mu_{\text{tr}} & l & 0 & 0 & 0 \\ \kappa_{\text{tr}} - \mu_{\text{tr}} & \kappa_{\text{tr}} + \mu_{\text{tr}} & l & 0 & 0 & 0 \\ l & l & n & 0 & 0 & 0 \\ 0 & 0 & 0 & \mu_{\text{tr}} & 0 & 0 \\ 0 & 0 & 0 & 0 & \mu_{\text{ax}} & 0 \\ 0 & 0 & 0 & 0 & 0 & \mu_{\text{ax}} \end{bmatrix} \begin{bmatrix} \varepsilon_{rr} \\ \varepsilon_{\theta\theta} \\ \varepsilon_{zz} \\ 2\varepsilon_{r\theta} \\ 2\varepsilon_{rz} \\ 2\varepsilon_{\theta z} \end{bmatrix} \quad \text{with} \quad \begin{aligned} \varepsilon_{rr} &= \frac{\partial u_r}{\partial r}, \\ \varepsilon_{\theta\theta} &= \frac{1}{r}\frac{\partial u_\theta}{\partial \theta} + \frac{u_r}{r}, \\ \varepsilon_{zz} &= \frac{\partial u_z}{\partial z}, \\ 2\varepsilon_{rz} &= \frac{\partial u_z}{\partial r} + \frac{\partial u_r}{\partial z}, \\ 2\varepsilon_{\theta z} &= \frac{1}{r}\frac{\partial u_z}{\partial \theta} + \frac{\partial u_\theta}{\partial z}, \\ 2\varepsilon_{r\theta} &= \frac{\partial u_\theta}{\partial r} + \frac{1}{r}\frac{\partial u_r}{\partial \theta} - \frac{u_\theta}{r}, \end{aligned} \tag{10}$$

and the equilibrium equations in the bulk read

$$\begin{cases} \dfrac{\partial \sigma_{rr}}{\partial r} + \dfrac{1}{r}\dfrac{\partial \sigma_{r\theta}}{\partial \theta} + \dfrac{\partial \sigma_{rz}}{\partial z} + \dfrac{\sigma_{rr} - \sigma_{\theta\theta}}{r} = 0, \\ \dfrac{\partial \sigma_{r\theta}}{\partial r} + \dfrac{1}{r}\dfrac{\partial \sigma_{\theta\theta}}{\partial \theta} + \dfrac{\partial \sigma_{\theta z}}{\partial z} + \dfrac{2}{r}\sigma_{r\theta} = 0, \\ \dfrac{\partial \sigma_{rz}}{\partial r} + \dfrac{1}{r}\dfrac{\partial \sigma_{\theta z}}{\partial \theta} + \dfrac{\partial \sigma_{zz}}{\partial z} + \dfrac{1}{r}\sigma_{rz} = 0. \end{cases} \tag{11}$$

The constitutive relations for the general interface at $r = r_1$ are characterized by four parameters for the traction jump ($\overline{m}$, $\overline{l}$, $\overline{n}$ and $\overline{\mu}_{\text{ax}}$) and three parameters for the displacement jump ($\overline{k}_r$, $\overline{k}_\theta$ and $\overline{k}_z$) as

$$\begin{bmatrix} \overline{\sigma}_{\theta\theta} \\ \overline{\sigma}_{zz} \\ \overline{\sigma}_{\theta z} \end{bmatrix} = \begin{bmatrix} \overline{m} & \overline{l} & 0 \\ \overline{l} & \overline{n} & 0 \\ 0 & 0 & \overline{\mu}_{\mathrm{ax}} \end{bmatrix} \begin{bmatrix} \overline{\varepsilon}_{\theta\theta} \\ \overline{\varepsilon}_{zz} \\ 2\overline{\varepsilon}_{\theta z} \end{bmatrix} \text{ with } \begin{aligned} \overline{\varepsilon}_{\theta\theta} &= \frac{1}{r_1}\frac{\partial \overline{u}_\theta}{\partial \theta} + \frac{\overline{u}_r}{r_1} \\ \overline{\varepsilon}_{zz} &= \frac{\partial \overline{u}_z}{\partial z} \\ 2\overline{\varepsilon}_{\theta z} &= \frac{1}{r_1}\frac{\partial \overline{u}_z}{\partial \theta} + \frac{\partial \overline{u}_\theta}{\partial z} \end{aligned} \text{ and } \begin{bmatrix} \overline{t}_r \\ \overline{t}_\theta \\ \overline{t}_z \end{bmatrix} = \begin{bmatrix} \overline{k}_r \, [\![u_r]\!] \\ \overline{k}_\theta \, [\![u_\theta]\!] \\ \overline{k}_z \, [\![u_z]\!] \end{bmatrix}. \tag{12}$$

The equilibrium equations at the interface are

$$\begin{cases} -\dfrac{\overline{\sigma}_{\theta\theta}}{r_1} + [\![\sigma_{rr}]\!] = 0\,, \\ \dfrac{1}{r_1}\dfrac{\partial \overline{\sigma}_{\theta\theta}}{\partial \theta} + \dfrac{\partial \overline{\sigma}_{\theta z}}{\partial z} + [\![\sigma_{r\theta}]\!] = 0\,, \\ \dfrac{1}{r_1}\dfrac{\partial \overline{\sigma}_{\theta z}}{\partial \theta} + \dfrac{\partial \overline{\sigma}_{zz}}{\partial z} + [\![\sigma_{rz}]\!] = 0\,. \end{cases} \tag{13}$$

The three normal vectors in cylindrical coordinates are

$$\boldsymbol{n}_r = \begin{bmatrix} \cos\theta \\ \sin\theta \\ 0 \end{bmatrix}, \quad \boldsymbol{n}_\theta = \begin{bmatrix} -\sin\theta \\ \cos\theta \\ 0 \end{bmatrix}, \quad \boldsymbol{n}_z = \begin{bmatrix} 0 \\ 0 \\ 1 \end{bmatrix}, \tag{14}$$

and therefore, the displacements and stresses can be represented in tensorial forms as

$$\begin{aligned} \boldsymbol{u} &= u_r\,\boldsymbol{n}_r + u_\theta\,\boldsymbol{n}_\theta + u_z\,\boldsymbol{n}_z\,, \\ \boldsymbol{\sigma} &= \sigma_{rr}\,\boldsymbol{n}_r \otimes \boldsymbol{n}_r + \sigma_{\theta\theta}\,\boldsymbol{n}_\theta \otimes \boldsymbol{n}_\theta + \sigma_{zz}\,\boldsymbol{n}_z \otimes \boldsymbol{n}_z + \frac{1}{2}\sigma_{r\theta}[\boldsymbol{n}_r \otimes \boldsymbol{n}_\theta + \boldsymbol{n}_\theta \otimes \boldsymbol{n}_r] \\ &\quad + \frac{1}{2}\sigma_{rz}[\boldsymbol{n}_r \otimes \boldsymbol{n}_z + \boldsymbol{n}_z \otimes \boldsymbol{n}_r] + \frac{1}{2}\sigma_{\theta z}[\boldsymbol{n}_\theta \otimes \boldsymbol{n}_z + \boldsymbol{n}_z \otimes \boldsymbol{n}_\theta]\,, \\ \overline{\boldsymbol{\sigma}} &= \overline{\sigma}_{\theta\theta}\,\boldsymbol{n}_\theta \otimes \boldsymbol{n}_\theta + \overline{\sigma}_{zz}\,\boldsymbol{n}_z \otimes \boldsymbol{n}_z + \frac{1}{2}\overline{\sigma}_{\theta z}[\boldsymbol{n}_\theta \otimes \boldsymbol{n}_z + \boldsymbol{n}_z \otimes \boldsymbol{n}_\theta]\,. \end{aligned} \tag{15}$$

Using the equilibrium equations in the bulk and on the interface, the divergence theorem for our problem can be written as

$$\begin{aligned} \int_{\mathcal{B}} \mathrm{div}\{\bullet\}\,\mathrm{d}V + \int_{\mathcal{I}} [\![\{\bullet\}]\!] \cdot \overline{\boldsymbol{n}}\,\mathrm{d}A &= \int_{\mathcal{S}} \{\bullet\} \cdot \boldsymbol{n}\,\mathrm{d}A \quad \text{and} \\ \int_{\mathcal{I}} \overline{\mathrm{div}}\{\bullet\}\,\mathrm{d}A - \int_{\mathcal{I}} \overline{\mathrm{div}}\overline{\boldsymbol{n}}\ \{\bullet\} \cdot \overline{\boldsymbol{n}}\,\mathrm{d}A &= \int_{\partial\mathcal{I}} \{\bullet\} \cdot \widetilde{\boldsymbol{n}}\,\mathrm{d}L\,, \end{aligned} \tag{16}$$

where $\widetilde{\boldsymbol{n}}$ is the normal at the boundary of the interface but along the interface itself. Using the above theorems, the average mechanical energy in the composite reads

$$\begin{aligned} U &= \frac{1}{2\mathscr{V}}\int_{\mathcal{B}} \boldsymbol{\sigma} : \boldsymbol{\varepsilon}\,\mathrm{d}V + \frac{1}{2\mathscr{V}}\int_{\mathcal{I}} \overline{\boldsymbol{\sigma}} : \overline{\boldsymbol{\varepsilon}}\,\mathrm{d}A \\ &= \frac{1}{2\mathscr{V}}\underbrace{\left[\int_{\mathcal{B}} \mathrm{div}(\boldsymbol{u} \cdot \boldsymbol{\sigma})\,\mathrm{d}V + \int_{\mathcal{I}} \overline{\boldsymbol{u}} \cdot [\![\boldsymbol{\sigma}]\!] \cdot \overline{\boldsymbol{n}}\,\mathrm{d}A\right]}_{\int_{\partial\mathcal{B}} [\boldsymbol{\sigma}\cdot\boldsymbol{n}]\cdot\boldsymbol{u}\,\mathrm{d}A} + \frac{1}{2\mathscr{V}}\underbrace{\int_{\mathcal{I}} \overline{\mathrm{div}}(\overline{\boldsymbol{u}} \cdot \overline{\boldsymbol{\sigma}})\,\mathrm{d}A}_{\int_{\partial\mathcal{I}} [\overline{\boldsymbol{\sigma}}\cdot\widetilde{\boldsymbol{n}}]\cdot\overline{\boldsymbol{u}}\,\mathrm{d}L}\,, \end{aligned} \tag{17}$$

The volume element in the cylindrical coordinates is $\mathrm{d}v = r\,\mathrm{d}r\,\mathrm{d}\theta\,\mathrm{d}z$, the (vertical) surface element at a constant radius r is $\mathrm{d}s_r = r\,\mathrm{d}\theta\,\mathrm{d}z$, the (horizontal) surface element at a constant height z is $\mathrm{d}s_z = r\,\mathrm{d}r\,\mathrm{d}\theta$ and

the line element at a constant radius r and height z is $\mathrm{d}l = r\,\mathrm{d}\theta$. Finally, the average mechanical energy in the RVE and in equivalent homogeneous medium read

$$
\begin{aligned}
U^{\mathrm{RVE}} &= \frac{1}{2\mathscr{V}}\int_0^{2\pi}\int_0^{r_2}\left[\left[\sigma_{rz}u_r+\sigma_{\theta z}u_\theta\sigma_{zz}u_z\right]_{z=L}-\left[\sigma_{rz}u_r+\sigma_{\theta z}u_\theta+\sigma_{zz}u_z\right]_{z=-L}\right]r\,\mathrm{d}r\,\mathrm{d}\theta\\
&\quad+\frac{1}{2\mathscr{V}}\int_{-L}^{L}\int_0^{2\pi}\left[\sigma_{rr}u_r+\sigma_{\theta r}u_\theta+\sigma_{zr}u_z\right]_{r=r_2}r_2\,\mathrm{d}\theta\,\mathrm{d}z\\
&\quad+\frac{1}{2\mathscr{V}}\int_0^{2\pi}\left[\left[\overline{\sigma}_{\theta z}\overline{u}_\theta+\overline{\sigma}_{zz}\overline{u}_z\right]_{z=L}-\left[\overline{\sigma}_{\theta z}\overline{u}_\theta+\overline{\sigma}_{zz}\overline{u}_z\right]_{z=-L}\right]_{r=r_1}r_1\,\mathrm{d}\theta\,,\\
U^{\mathrm{eq}} &= \frac{1}{2\mathscr{V}}\int_0^{2\pi}\int_0^{r_2}\left[\left[\sigma^{\mathrm{eq}}_{rz}u^{\mathrm{eq}}_r+\sigma^{\mathrm{eq}}_{\theta z}u^{\mathrm{eq}}_\theta+\sigma^{\mathrm{eq}}_{zz}u^{\mathrm{eq}}_z\right]_{z=L}-\left[\sigma^{\mathrm{eq}}_{rz}u^{\mathrm{eq}}_r+\sigma^{\mathrm{eq}}_{\theta z}u^{\mathrm{eq}}_\theta+\sigma^{\mathrm{eq}}_{zz}u^{\mathrm{eq}}_z\right]_{z=-L}\right]r\,\mathrm{d}r\,\mathrm{d}\theta\\
&\quad+\frac{1}{2\mathscr{V}}\int_{-L}^{L}\int_0^{2\pi}\left[\sigma^{\mathrm{eq}}_{rr}u^{\mathrm{eq}}_r+\sigma^{\mathrm{eq}}_{\theta r}u^{\mathrm{eq}}_\theta+\sigma^{\mathrm{eq}}_{zr}u^{\mathrm{eq}}_z\right]_{r=r_2}r_2\mathrm{d}\theta\,\mathrm{d}z\,.
\end{aligned}
\tag{18}
$$

As we will see later, for the expansion and the in-plane shear boundary value problems, all the quantities with index z vanish and the above relations simplify to

$$
\begin{aligned}
U^{\mathrm{RVE}} &= \frac{1}{4\pi r_2^2 L}\int_{-L}^{L}\int_0^{2\pi}\left[\sigma^{(2)}_{rr}\,u^{(2)}_r+\sigma^{(2)}_{r\theta}\,u^{(2)}_\theta\right]_{r=r_2}r_2\,\mathrm{d}\theta\,\mathrm{d}z\,,\\
U^{\mathrm{eq}} &= \frac{1}{4\pi r_2^2 L}\int_{-L}^{L}\int_0^{2\pi}\left[\sigma^{\mathrm{eq}}_{rr}\,u^{\mathrm{eq}}_r+\sigma^{\mathrm{eq}}_{r\theta}\,u^{\mathrm{eq}}_\theta\right]_{r=r_2}r_2\,\mathrm{d}\theta\,\mathrm{d}z\,.
\end{aligned}
\tag{19}
$$

3.2 Composite cylinder assemblage (CCA) approach and generalized self-consistent method (GSCM)

Recently, Chatzigeorgiou et al. [65] proposed an extension of the generalized self-consistent method (GSCM) [106] and the composite cylinders assemblage (CCA) approach [107] to determine the effective shear modulus and bulk modulus of fiber composites embedding general interfaces. Motivated by these observations, here the original formalism of Hashin and Rosen [107] is extended to account for the general interface to determine bounds on the overall shear modulus ${}^{\mathrm{M}}\mu$. Note that the same methodology can be employed to obtain bounds for the effective bulk modulus ${}^{\mathrm{M}}\kappa$. However, the upper and lower bounds on the bulk modulus coincide. Therefore, the bounds and estimates for the bulk modulus yield identical results. The derivations of the effective bulk and shear modulus developed in [65] are briefly (and more explicitly) stated here for the sake of completeness.

3.2.1 Effective bulk modulus

Assume that the RVE is subject to a radial expansion with its upper and lower surfaces fixed as depicted in Fig. 5 (left). The displacement field in cylindrical coordinates reads

$$
\boldsymbol{u}^0_{(r,\theta,z)} = \begin{bmatrix}\beta r\\ 0\\ 0\end{bmatrix}\,. \tag{20}
$$

Hashin and Rosen showed that the displacement field within each constituent reads

$$
u^{(i)}_r = \beta\,\Xi^{(i)}_1 r+\beta\,\Xi^{(i)}_2\frac{1}{r}\qquad\text{and}\qquad u^{(i)}_\theta = u^{(i)}_z = 0\,, \tag{21}
$$

for $i=1,2$ where $i=1$ corresponds to the fiber and $i=2$ corresponds to the matrix. The unknowns $\Xi^{(1)}_1$, $\Xi^{(2)}_1$, $\Xi^{(1)}_2$ and $\Xi^{(2)}_2$ can be calculated using the boundary and interface conditions

$$
\begin{aligned}
&u^{(1)}_r \text{ finite at } r=0 \;\rightarrow\; && \Xi^{(1)}_2 = 0\,, && \text{(finite displacement at } r=0)\\
&\overline{t}_r = \overline{k}_r\,[\![u_r]\!] \;\rightarrow\; && \frac{\sigma^{(2)}_{rr}(r_1)+\sigma^{(1)}_{rr}(r_1)}{2} = \overline{k}\left[u^{(2)}_r(r_1)-u^{(1)}_r(r_1)\right], && \text{(traction average at } r=r_1)\\
&\left[\overline{\operatorname{div}\,\sigma}\right]_r+[\![t_r]\!]=0 \;\rightarrow\; && -\frac{\overline{\sigma}_{\theta\theta}}{r_1}+\sigma^{(2)}_{rr}(r_1)-\sigma^{(1)}_{rr}(r_1)=0\,, && \text{(traction equilibrium at } r=r_1)\\
&u^{(2)}_r(r_2)=\beta r_2\,, && && \text{(prescribed displacement at } r=r_2)
\end{aligned}
\tag{22}
$$

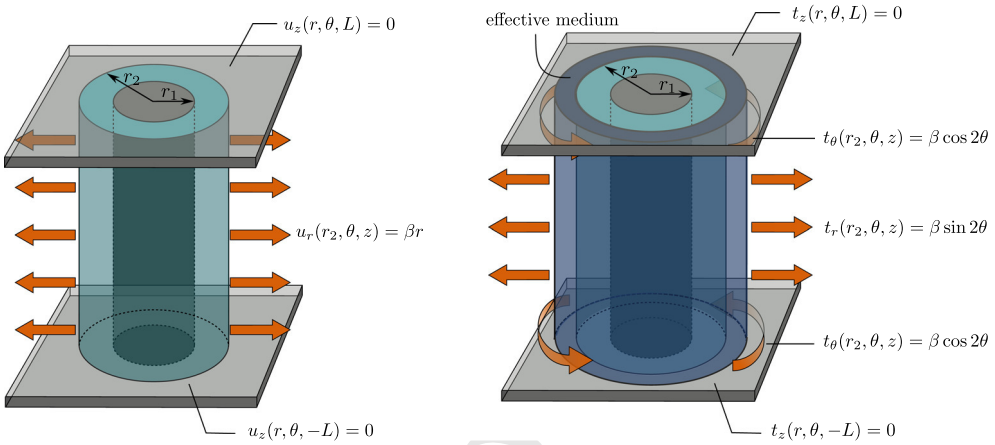

Fig. 5 Boundary value problems for obtaining the macroscopic bulk modulus (left) and the macroscopic shear modulus (right) developed in [65]

leading to the system

$$\begin{bmatrix} 0 & 1 & \dfrac{1}{r_2^2} \\ -\lambda_1-\mu_1-\dfrac{\overline{\mu}}{2r_1} & \lambda_2+\mu_2-\dfrac{\overline{\mu}}{2r_1} & -\dfrac{2\mu_2 r_1+\overline{\mu}}{2r_1^3} \\ \dfrac{\lambda_1+\mu_1}{\overline{k}}+r_1 & \dfrac{\lambda_2+\mu_2}{\overline{k}}-r_1 & -\dfrac{\mu_2+\overline{k}r_1}{\overline{k}r_1^2} \end{bmatrix} \begin{bmatrix} \Xi_1^{(1)} \\ \Xi_1^{(2)} \\ \Xi_2^{(2)} \end{bmatrix} = \begin{bmatrix} 1 \\ 0 \\ 0 \end{bmatrix}. \tag{23}$$

If the RVE is substituted by an equivalent homogeneous medium, applying the boundary condition (20) yields the displacement field $u_r^{\mathrm{eq}}=\beta r$ and $u_\theta^{\mathrm{eq}}=u_z^{\mathrm{eq}}=0$. Using Eq. (19), the overall energy in the RVE and in the equivalent homogeneous medium reads

$$U^{\mathrm{RVE}}=2\beta^2\left[\Xi_1^{(2)}[\lambda_2+\mu_2]-\frac{\Xi_2^{(2)}\mu_2}{r_2^2}\right] \quad \text{and} \quad U^{\mathrm{eq}}=2\beta^{2\mathrm{M}}\kappa\,, \tag{24}$$

where $\Xi_1^{(2)}$ and $\Xi_2^{(2)}$ are the solutions of the system (23). The above energies should be equal according to Hill–Mandel condition. Therefore, we can obtain an explicit expression for the overall bulk modulus ${}^{\mathrm{M}}\kappa$ of fiber composites embedding general interfaces

$${}^{\mathrm{M}}\kappa=\lambda_2+\mu_2+\frac{f}{\dfrac{1}{\dfrac{\left[2r_1\lambda_1+2r_1\mu_1+\overline{\mu}\right]\left[2\overline{k}r_1^2-\overline{\mu}\right]}{4r_1^2\left[2\lambda_1+2\mu_1+\overline{k}r_1\right]+2r_1\overline{\mu}}-\left[\lambda_2+\mu_2\right]+\dfrac{\overline{\mu}}{2r_1}}+\dfrac{1-f}{\lambda_2+2\mu_2}}\,. \tag{25}$$

3.2.2 Effective shear modulus

In order to determine the effective shear modulus of fiber composites, Christensen and Lo [106] proposed to consider an infinite effective medium surrounding the matrix whose properties are indeed, the unknowns of the problem. Therefore, the composite cylinder assemblage approach is transformed to generalized self-consistent method (GSCM). To obtain the effective shear modulus, the deviatoric traction is applied to the RVE as depicted in Fig. 5 (right). The traction field in cylindrical coordinates reads

$$\boldsymbol{t}^0_{(r,\theta,z)}=\begin{bmatrix} \beta\sin 2\theta \\ \beta\cos 2\theta \\ 0 \end{bmatrix}. \tag{26}$$

Considering the above boundary value problem and following the procedures in [106], the developed displacement fields in the medium read

$$
\begin{aligned}
u_r^{(i)} &= \sum_{j=1}^{4} a_j^{(i)}\,\Xi_j^{(i)} r^{n_j^{(i)}}\,\sin(2\theta)\,, \qquad u_\theta^{(i)} = \sum_{j=1}^{4} \Xi_j^{(i)} r^{n_j^{(i)}}\,\cos(2\theta)\,,\\
u_r^{(\mathrm{eff})} &= \beta\frac{r_2}{4^{\mathrm{M}}\mu}\left[\frac{2r}{r_2} + \Xi_3^{(\mathrm{eff})}\frac{r_2^3}{r^3} + 2\left[1+\frac{^{\mathrm{M}}\mu}{^{\mathrm{M}}\kappa}\right]\Xi_4^{(\mathrm{eff})}\frac{r_2}{r}\right]\sin(2\theta)\,,\\
u_\theta^{(\mathrm{eff})} &= \beta\frac{r_2}{4^{\mathrm{M}}\mu}\left[\frac{2r}{r_2} - \Xi_3^{(\mathrm{eff})}\frac{r_2^3}{r^3} + 2\frac{^{\mathrm{M}}\mu}{^{\mathrm{M}}\kappa}\Xi_4^{(\mathrm{eff})}\frac{r_2}{r}\right]\cos(2\theta)\,,
\end{aligned}
\tag{27}
$$

for $i = 1, 2$ where $i = 1$ corresponds to the fiber and $i = 2$ corresponds to the matrix. The constants $a_j^{(i)}$ read

$$
a_j^{(i)} = \frac{2\lambda^{(i)} + 6\mu^{(i)} - 2n_j^{(i)}[\lambda^{(i)} + \mu^{(i)}]}{\lambda^{(i)} + 6\mu^{(i)} + [n_j^{(i)}]^2[\lambda^{(i)} + 2\mu^{(i)}]}\,,
\tag{28}
$$

with $n_j^{(i)}$ being the solutions of the polynomial $n^4 - 10n^2 + 9 = 0$. The constants $n_1^{(i)}$ and $n_2^{(i)}$ are taken to be the positive solutions, and $n_3^{(i)}$ and $n_4^{(i)}$ are taken to be the negative solutions as $n_1^{(i)} = 3$, $n_2^{(i)} = 1$, $n_3^{(i)} = -3$ and $n_4^{(i)} = -1$. The ten unknowns $\Xi_1^{(1)}$, $\Xi_2^{(1)}$, $\Xi_3^{(1)}$, $\Xi_4^{(1)}$, $\Xi_1^{(2)}$, $\Xi_2^{(2)}$, $\Xi_3^{(2)}$, $\Xi_4^{(2)}$, $\Xi_3^{(\mathrm{eff})}$ and $\Xi_4^{(\mathrm{eff})}$ can be determined via applying the interface and boundary conditions. The boundary and interface conditions that hold for the RVE in this problem are

$$
\begin{aligned}
&u_r^{(1)},\ u_\theta^{(1)} \text{ finite at } r=0 \rightarrow && \Xi_3^{(1)} = \Xi_4^{(1)} = 0\,, && \text{(finite displacement at } r=0)\\
&\bar{t}_r = \bar{k}_r\,[\![u_r]\!] && \rightarrow\ \sigma_{rr}^{(2)}(r_1) + \sigma_{rr}^{(1)}(r_1) = 2\bar{k}_r\left[u_r^{(2)}(r_1) - u_r^{(1)}(r_1)\right]\,, && \text{(traction average at } r=r_1)\\
&\bar{t}_\theta = \bar{k}_\theta\,[\![u_\theta]\!] && \rightarrow\ \sigma_{r\theta}^{(2)}(r_1) + \sigma_{r\theta}^{(1)}(r_1) = 2\bar{k}_\theta\left[u_\theta^{(2)}(r_1) - u_\theta^{(1)}(r_1)\right]\,, && \text{(traction average at } r=r_1)\\
&\left[\overline{\mathrm{div}}\,\bar{\sigma}\right]_r + [\![t_r]\!] = 0 && \rightarrow\ -\frac{\bar{\sigma}_{\theta\theta}}{r_1} + \sigma_{rr}^{(2)}(r_1) - \sigma_{rr}^{(1)}(r_1) = 0\,, && \text{(traction equilibrium at } r=r_1)\\
&\left[\overline{\mathrm{div}}\,\bar{\sigma}\right]_\theta + [\![t_\theta]\!] = 0 && \rightarrow\ \frac{1}{r_1}\frac{\partial\bar{\sigma}_{\theta\theta}}{\partial\theta} + \sigma_{r\theta}^{(2)}(r_1) - \sigma_{r\theta}^{(1)}(r_1) = 0\,, && \text{(traction equilibrium at } r=r_1)\\
&\sigma_{rr}^{(2)}(r_2) = \sigma_{rr}^{(\mathrm{eff})}(r_2) && \text{and}\ \ \sigma_{r\theta}^{(2)}(r_2) = \sigma_{r\theta}^{(\mathrm{eff})}(r_2)\,, && \text{(traction continuity at } r=r_2)\\
&u_r^{(2)}(r_2) = u_r^{(\mathrm{eff})}(r_2) && \text{and}\ \ u_\theta^{(2)}(r_2) = u_\theta^{(\mathrm{eff})}(r_2)\,. && \text{(displacement continuity at } r=r_2).
\end{aligned}
\tag{29}
$$

In order to find the unknowns using the above system of equations, an additional energetic criterion expressed in [106] must be imposed which is deduced from the Eshelby's energy principle

$$
\int_0^{2\pi}\left[\sigma_{rr}^{(\mathrm{eff})}u_r^{\mathrm{eq}} + \sigma_{r\theta}^{(\mathrm{eff})}u_\theta^{\mathrm{eq}} - \sigma_{rr}^{\mathrm{eq}}u_r^{(\mathrm{eff})} - \sigma_{r\theta}^{\mathrm{eq}}u_\theta^{(\mathrm{eff})}\right]_{r=r_2}\mathrm{d}\theta = 0\,,
\tag{30}
$$

which yields $\Xi_4^{(\mathrm{eff})} = 0$. The remaining unknowns are calculated by solving the system (29). Further details regarding the solution of the system are available in Appendix A.1. Unlike the effective bulk modulus, it is not possible to furnish an explicit expression for the effective shear modulus. Nevertheless, a semi-explicit expression is attainable which reads

$$
[a_6b_5 - a_5b_6]^{\mathrm{M}}\mu^2 - [b_5c_5 - b_6c_5 + a_5c_6 + a_6c_6]^{\mathrm{M}}\mu + 2c_5c_6 = 0\,.
$$

Between the two roots obtained from the above relation, the positive one is the effective shear modulus. The parameters a_5, a_6, b_5, b_6, c_5 and c_6 are obtained from Eq. (A.5), see Apeendix A.1 for more details.

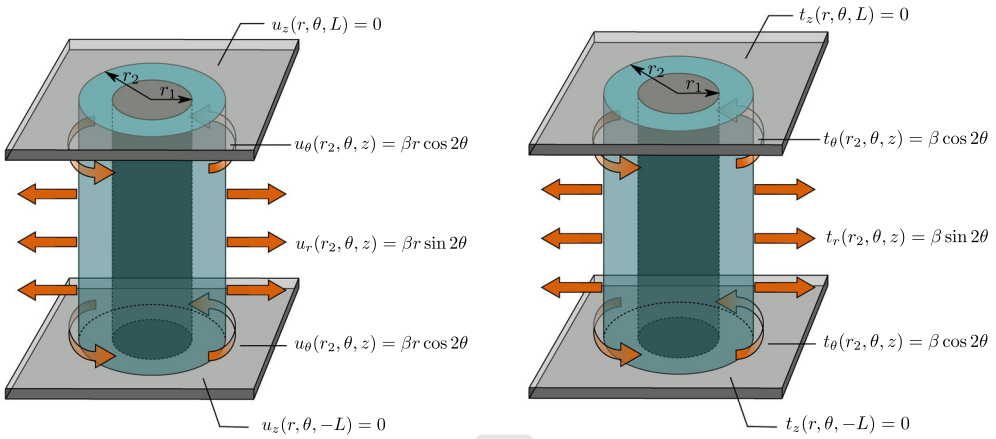

Fig. 6 Boundary value problems for obtaining bounds on the macroscopic shear modulus of a fiber composite. Strain boundary condition (left) and stress boundary condition (right)

3.2.3 Strain bound on the shear modulus

To obtain the strain bound on the overall in-plane shear modulus, shear displacement is applied on the boundary of the RVE as shown in Fig. 6 (left) which reads

$$\boldsymbol{u}^0_{(r,\theta,z)} = \begin{bmatrix} \beta r\sin 2\theta \\ \beta r\cos 2\theta \\ 0 \end{bmatrix}. \tag{31}$$

Similar to the previous case, the developed displacement fields in the medium result in the analytical form

$$u_r^{(i)} = \sum_{j=1}^{4} a_j^{(i)}\,\Xi_j^{(i)}\,r^{n_j^{(i)}}\sin(2\theta)\,,\quad u_\theta^{(i)} = \sum_{j=1}^{4} \Xi_j^{(i)}\,r^{n_j^{(i)}}\cos(2\theta)\,, \tag{32}$$

where the superscripts $i=1,2$ correspond to the fiber and matrix, respectively. The constants $a_j^{(i)}$ are obtained similar to Eq. (28).

The eight unknowns $\Xi_1^{(1)}$, $\Xi_2^{(1)}$, $\Xi_3^{(1)}$, $\Xi_4^{(1)}$, $\Xi_1^{(2)}$, $\Xi_2^{(2)}$, $\Xi_3^{(2)}$ and $\Xi_4^{(2)}$ can be determined via applying the boundary and interface conditions which read

$$\begin{aligned}
&u_r^{(1)},\ u_\theta^{(1)} \text{ finite at } r=0 \ \rightarrow\ && \Xi_3^{(1)}=\Xi_4^{(1)}=0\,, && \text{(finite displacement at } r=0)\\
&\bar{t}_r=\bar{k}_r\,[\![u_r]\!] \ \rightarrow\ && \sigma_{rr}^{(2)}(r_1)+\sigma_{rr}^{(1)}(r_1)=2\bar{k}_r\left[u_r^{(2)}(r_1)-u_r^{(1)}(r_1)\right], && \text{(traction average at } r=r_1)\\
&\bar{t}_\theta=\bar{k}_\theta\,[\![u_\theta]\!] \ \rightarrow\ && \sigma_{r\theta}^{(2)}(r_1)+\sigma_{r\theta}^{(1)}(r_1)=2\bar{k}_\theta\left[u_\theta^{(2)}(r_1)-u_\theta^{(1)}(r_1)\right], && \text{(traction average at } r=r_1)\\
&\left[\overline{\operatorname{div}\sigma}\right]_r+[\![t_r]\!]=0 \ \rightarrow\ && -\frac{\overline{\sigma}_{\theta\theta}}{r_1}+\sigma_{rr}^{(2)}(r_1)-\sigma_{rr}^{(1)}(r_1)=0\,, && \text{(traction equilibrium at } r=r_1)\\
&\left[\overline{\operatorname{div}\sigma}\right]_\theta+[\![t_\theta]\!]=0 \ \rightarrow\ && \frac{1}{r_1}\frac{\partial\overline{\sigma}_{\theta\theta}}{\partial\theta}+\sigma_{r\theta}^{(2)}(r_1)-\sigma_{r\theta}^{(1)}(r_1)=0\,, && \text{(traction equilibrium at } r=r_1)\\
&u_r^{(2)}(r_2)=\beta r_2\sin(2\theta) \ \text{ and } \ u_\theta^{(2)}(r_2)=\beta r_2\cos(2\theta)\,. && && \text{(boundary condition at } r=r_2)\,.
\end{aligned} \tag{33}$$

Further details regarding the construction of the system of equations are available in Appendix A.2. For an equivalent homogeneous medium with the same boundary conditions, the displacement field reads $u_r^{\mathrm{eq}}(r) = \beta r\sin(2\theta)$ and $u_\theta^{\mathrm{eq}}(r) = \beta r\cos(2\theta)$. Having the stress and displacement fields, using Eq. (19), one can

calculate the average mechanical energy in the RVE and in the equivalent homogeneous medium

$$U^{\mathrm{RVE}} = \frac{\beta^2}{2}\left[\frac{6\mu_2[\lambda_2+\mu_2]r_2^2}{2\lambda_2+3\mu_2}\,\Xi_1^{(2)} + 4\mu_2\,\Xi_2^{(2)} - \frac{2[\lambda_2+\mu_2]}{r_2^2}\,\Xi_4^{(2)}\right], \qquad U^{\mathrm{eq}} = 2\beta^2\,{}^{\mathrm{M}}\mu\,. \tag{34}$$

Considering $U^{\mathrm{RVE}} = U^{\mathrm{eq}}$ results in a semi-explicit expression for the strain bound on the effective in-plane shear modulus

$${}^{\mathrm{M}}\mu_{\mathrm{strain}} = \frac{1}{4}\left[\frac{6\mu_2[\lambda_2+\mu_2]r_2^2}{2\lambda_2+3\mu_2}\,\Xi_1^{(2)} + 4\mu_2\,\Xi_2^{(2)} - \frac{2[\lambda_2+\mu_2]}{r_2^2}\,\Xi_4^{(2)}\right]. \tag{35}$$

where $\Xi_1^{(2)}$, $\Xi_2^{(2)}$, $\Xi_3^{(2)}$ and $\Xi_4^{(2)}$ are the solution of the system of equations (A.6).

3.2.4 Stress bound on the shear modulus

Following the same methodology for the boundary value problem of Fig. 6 (right), the stress bound on the macroscopic in-plane shear modulus can be obtained. Consider an RVE subject to the traction field

$$\boldsymbol{t}^0_{(r,\theta,z)} = \begin{bmatrix} \beta\sin 2\theta \\ \beta\cos 2\theta \\ 0 \end{bmatrix}. \tag{36}$$

The displacement fields in the constituents due to this boundary conditions are similar to Eq. (32). The eight unknowns $\Xi_1^{(1)}$, $\Xi_2^{(1)}$, $\Xi_3^{(1)}$, $\Xi_4^{(1)}$, $\Xi_1^{(2)}$, $\Xi_2^{(2)}$, $\Xi_3^{(2)}$ and $\Xi_4^{(2)}$ can be determined via applying the boundary and interface conditions which read

$$\begin{aligned}
&u_r^{(1)},\, u_\theta^{(1)} \text{ finite at } r=0 \;\rightarrow\; && \Xi_3^{(1)} = \Xi_4^{(1)} = 0\,, && \text{(finite displacement at } r=0)\\
&\bar{t}_r = \bar{k}_r\,[\![u_r]\!] \;\rightarrow\; && \sigma_{rr}^{(2)}(r_1) + \sigma_{rr}^{(1)}(r_1) = 2\bar{k}_r\left[u_r^{(2)}(r_1) - u_r^{(1)}(r_1)\right], && \text{(traction average at } r=r_1)\\
&\bar{t}_\theta = \bar{k}_\theta\,[\![u_\theta]\!] \;\rightarrow\; && \sigma_{r\theta}^{(2)}(r_1) + \sigma_{r\theta}^{(1)}(r_1) = 2\bar{k}_\theta\left[u_\theta^{(2)}(r_1) - u_\theta^{(1)}(r_1)\right], && \text{(traction average at } r=r_1)\\
&\left[\overline{\mathrm{div}}\,\bar{\sigma}\right]_r + [\![t_r]\!] = 0 \;\rightarrow\; && -\frac{\bar{\sigma}_{\theta\theta}}{r_1} + \sigma_{rr}^{(2)}(r_1) - \sigma_{rr}^{(1)}(r_1) = 0\,, && \text{(traction equilibrium at } r=r_1)\\
&\left[\overline{\mathrm{div}}\,\bar{\sigma}\right]_\theta + [\![t_\theta]\!] = 0 \;\rightarrow\; && \frac{1}{r_1}\frac{\partial\bar{\sigma}_{\theta\theta}}{\partial\theta} + \sigma_{r\theta}^{(2)}(r_1) - \sigma_{r\theta}^{(1)}(r_1) = 0\,, && \text{(traction equilibrium at } r=r_1)\\
&\sigma_{rr}^{(2)}(r_2) = \beta\sin(2\theta) \quad \text{and} \quad && \sigma_{r\theta}^{(2)}(r_2) = \beta\cos(2\theta)\,. && \text{(boundary condition at } r=r_2)\,.
\end{aligned} \tag{37}$$

Further details regarding the construction of the system of equations are available in Appendix A.3. For an equivalent homogeneous medium with the same boundary conditions, the displacement field reads

$$u_r^{\mathrm{eq}}(r) = \frac{\beta}{2^{\mathrm{M}}\mu} r\sin(2\theta)\,, \qquad u_\theta^{\mathrm{eq}}(r) = \frac{\beta}{2^{\mathrm{M}}\mu} r\cos(2\theta)\,, \qquad u_z^{\mathrm{eq}}(r) = 0. \tag{38}$$

Using Eq. (19), the same strategy can be employed to define the energy stored in the RVE and the equivalent homogeneous medium.

$$U^{\mathrm{RVE}} = \frac{\beta^2}{2}\left[\frac{3[\lambda_2+\mu_2]r_2^2}{2\lambda_2+3\mu_2}\,\Xi_1^{(2)} + 2\Xi_2^{(2)} + \frac{\lambda_2+3\mu_2}{\mu_2 r_2^2}\,\Xi_4^{(2)}\right], \qquad U^{\mathrm{eq}} = \frac{\beta^2}{2^{\mathrm{M}}\mu}\,. \tag{39}$$

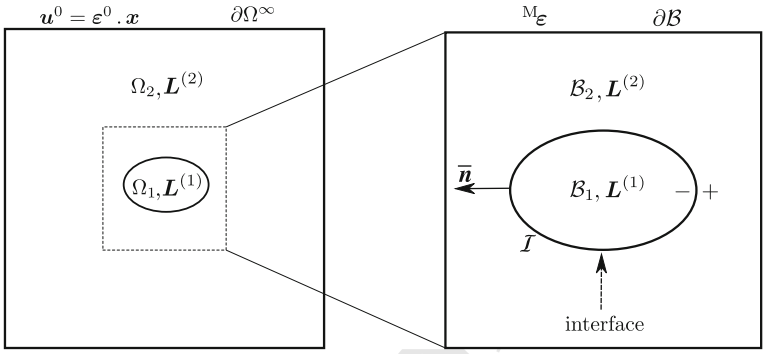

Fig. 7 Illustration of inhomogeneity with general interface inside an infinite matrix (left) and RVE of fiber composite with general interface (right)

Considering $U^{\mathrm{RVE}} = U^{\mathrm{eq}}$ results in a semi-explicit expression for the stress bound on the effective in-plane shear modulus

$$^{\mathrm{M}}\mu_{\mathrm{stress}} = \left[\frac{3[\lambda_2 + \mu_2]r_2^2}{2\lambda_2 + 3\mu_2} \Xi_1^{(2)} + 2\Xi_2^{(2)} + \frac{\lambda_2 + 3\mu_2}{\mu_2 r_2^2} \Xi_4^{(2)} \right]^{-1} . \tag{40}$$

where $\Xi_1^{(2)}$, $\Xi_2^{(2)}$, $\Xi_3^{(2)}$ and $\Xi_4^{(2)}$ are the solution of the system of equations (A.7).

3.3 Modified Mori–Tanaka method

Analytical estimates for the effective properties of fiber composites with general interfaces have been developed in [65]. Using energy principles, Duan et al. [108] proposed to substitute the fiber/interface system with an equivalent fiber to predict the overall behavior of the medium. Both methodologies provide reasonable estimates compared to full field homogenization strategies, like the periodic homogenization framework, but they cannot provide information about the local fields that are developed in various phases of the medium, including the interface. *Our new methodology here not only obtains the effective properties, but also defines the concentration tensors in each phase*. The primary advantage of the concentration tensors is that they link the macroscopic fields with the average fields in the matrix, fiber and interface hence, furnishing better insights into the microstructural response of composites. For composites with interfaces, the main idea is to identify the global interaction tensors for the fiber/interface system by solving the Eshelby's inhomogeneity problem [109]. Such investigation is motivated by similar techniques in the literature for coated particles or fibers [98,110–112]. Note the Mori–Tanaka estimates can lose major symmetry and thus results in physically meaningless estimates. However, the loss of symmetry in the Mori–Tanaka estimates appears in composites with different shapes of fibers, or fibers of the same shape but different orientation (non-uniform orientation distribution function). For aligned long fiber composites, it has been shown analytically that Mori–Tanaka continues to produce effective properties that respect the major symmetry [113]. This limitation of the Mori–Tanaka estimates holds regardless of interfaces.

3.3.1 General framework

Figure 7 (left) illustrates an inhomogeneity with general ellipsoidal shape occupying the space Ω_1 with elasticity modulus $\boldsymbol{L}^{(1)}$ surrounded by a general interface $\mathcal{I}$. An infinite matrix occupying the space Ω_2 with elasticity tensor $\boldsymbol{L}^{(2)}$ is embedding the inhomogeneity/interface system. The matrix is subjected to a far field linear displacement condition $\boldsymbol{u}^0 = \boldsymbol{\varepsilon}^0 \cdot \boldsymbol{x}$. The equilibrium equations throughout the medium are given in Eq. (4) and further detailed in [65].

In this contribution, similar to [108] we propose to treat the fiber/interface system as a unique phase, but instead of identifying the response, we identify a strain interaction tensor $\boldsymbol{T}$ and a stress–strain interaction tensor $\boldsymbol{H}$ as

$$\langle \boldsymbol{\varepsilon} \rangle_{\Omega_1}^{+} = \boldsymbol{T} : \boldsymbol{\varepsilon}^0 = \frac{1}{2|\Omega_1|} \int_{\mathcal{I}} [\boldsymbol{u}^{+} \otimes \overline{\boldsymbol{n}} + \overline{\boldsymbol{n}} \otimes \boldsymbol{u}^{+}] \, \mathrm{d}A \quad \text{and}$$

$$\langle\boldsymbol{\sigma}\rangle^{+}_{\Omega_1} = \boldsymbol{H}:\boldsymbol{\varepsilon}^0 = \frac{1}{|\Omega_1|}\int_{\Omega_1}\boldsymbol{\sigma}^-\,\mathrm{d}V + \frac{1}{|\Omega_1|}\int_{\mathcal{I}}\overline{\boldsymbol{\sigma}}\,\mathrm{d}A\,. \tag{41}$$

In addition, one can identify the pure fiber's concentration tensor as

$$\langle\boldsymbol{\varepsilon}\rangle^{-}_{\Omega_1} = \boldsymbol{T}^{(1)}:\boldsymbol{\varepsilon}^0 = \frac{1}{2|\Omega_1|}\int_{\mathcal{I}}[\boldsymbol{u}^-\otimes\overline{\boldsymbol{n}} + \overline{\boldsymbol{n}}\otimes\boldsymbol{u}^-]\,\mathrm{d}A\,. \tag{42}$$

More precisely, $\langle\boldsymbol{\varepsilon}\rangle^{-}_{\Omega_1}$ corresponds to the strain field in the fiber itself, whereas $\langle\boldsymbol{\varepsilon}\rangle^{+}_{\Omega_1}$ corresponds to the strain field in the fiber/interface system. This case study is an extension of the Eshelby's inhomogeneity problem, and the tensors $\boldsymbol{T}$ and $\boldsymbol{H}$ are extremely useful to develop the mean-field theories for composites [98]. Consider a RVE of fiber composite with the volume of $\mathscr{V}$ and the boundary of $\partial\mathcal{B}$ occupying the space $\mathcal{B}$ shown in Fig. 7 (right). The RVE is subjected to a macroscopic strain ${}^{\mathrm{M}}\boldsymbol{\varepsilon}$. The fiber with the volume of $\mathscr{V}_1$ occupies the space $\mathcal{B}_1$, and the matrix with the volume of $\mathscr{V}_2$ occupies the space $\mathcal{B}_2$. Obviously, $\mathcal{B} = \mathcal{B}_1\cup\mathcal{B}_2$ and $\mathscr{V} = \mathscr{V}_1 + \mathscr{V}_2$. The fiber volume fraction is $f = \mathscr{V}_1/\mathscr{V}$, and accordingly, Eq. (7) can be rewritten as

$$\begin{aligned}
{}^{\mathrm{M}}\boldsymbol{\varepsilon} &= \frac{1}{\mathscr{V}}\int_{\mathcal{B}}\boldsymbol{\varepsilon}\,\mathrm{d}V + \frac{1}{2\mathscr{V}}\int_{\mathcal{I}}\big[[\![\boldsymbol{u}]\!]\otimes\overline{\boldsymbol{n}} + \overline{\boldsymbol{n}}\otimes[\![\boldsymbol{u}]\!]\big]\,\mathrm{d}A = [1-f]\boldsymbol{\varepsilon}^{(2)} + f\boldsymbol{\varepsilon}^{(1)} + \widehat{\boldsymbol{\varepsilon}}\,,\\
{}^{\mathrm{M}}\boldsymbol{\sigma} &= \frac{1}{\mathscr{V}}\int_{\mathcal{B}}\boldsymbol{\sigma}\,\mathrm{d}V + \frac{1}{\mathscr{V}}\int_{\mathcal{I}}\overline{\boldsymbol{\sigma}}\,\mathrm{d}A = [1-f]\boldsymbol{L}^{(2)}:\boldsymbol{\varepsilon}^{(2)} + f\boldsymbol{L}^{(1)}:\boldsymbol{\varepsilon}^{(1)} + \widehat{\boldsymbol{\sigma}}\,,
\end{aligned} \tag{43}$$

in which

$$\boldsymbol{\varepsilon}^{(1)} = \frac{1}{\mathscr{V}_1}\int_{\mathcal{B}_1}\boldsymbol{\varepsilon}\,\mathrm{d}V\,,\qquad \boldsymbol{\varepsilon}^{(2)} = \frac{1}{\mathscr{V}_2}\int_{\mathcal{B}_2}\boldsymbol{\varepsilon}\,\mathrm{d}V \qquad\text{and}\qquad \widehat{\boldsymbol{\varepsilon}} = \frac{1}{2\mathscr{V}}\int_{\mathcal{I}}\Big[[\![\boldsymbol{u}]\!]\otimes\overline{\boldsymbol{n}} + \overline{\boldsymbol{n}}\otimes[\![\boldsymbol{u}]\!]\Big]\,\mathrm{d}A\,, \tag{44}$$

are the average strains in the fiber, matrix and interface, respectively. The average stress on the interface reads

$$\widehat{\boldsymbol{\sigma}} = \frac{1}{\mathscr{V}}\int_{\mathcal{I}}\overline{\boldsymbol{\sigma}}\,\mathrm{d}A\,. \tag{45}$$

Exploiting the interaction tensors (41) and (42), the Mori–Tanaka scheme reads

$$\boldsymbol{\varepsilon}^{(1)} = \boldsymbol{T}^{(1)}:\boldsymbol{\varepsilon}^{(2)}\,,\qquad \boldsymbol{\varepsilon}^{(1)} + \frac{1}{f}\widehat{\boldsymbol{\varepsilon}} = \boldsymbol{T}:\boldsymbol{\varepsilon}^{(2)}\,,\qquad \boldsymbol{L}^{(1)}:\boldsymbol{\varepsilon}^{(1)} + \frac{1}{f}\widehat{\boldsymbol{\sigma}} = \boldsymbol{H}:\boldsymbol{\varepsilon}^{(2)}\,. \tag{46}$$

Thus, Eq. $(43)_1$ yields

$${}^{\mathrm{M}}\boldsymbol{\varepsilon} = \Big[[1-f]\mathbb{I} + f\boldsymbol{T}\Big]:\boldsymbol{\varepsilon}^{(2)} \qquad\text{or}\qquad \boldsymbol{\varepsilon}^{(2)} = \boldsymbol{A}^{(2)}:{}^{\mathrm{M}}\boldsymbol{\varepsilon}\,, \tag{47}$$

where $\mathbb{I}$ is the fourth-order identity tensor and $\boldsymbol{A}^{(2)} = [[1-f]\mathbb{I} + f\boldsymbol{T}]^{-1}$. On the other hand, Eq. $(43)_2$ yields

$${}^{\mathrm{M}}\boldsymbol{\sigma} = \Big[[1-f]\boldsymbol{L}^{(2)} + f\boldsymbol{H}\Big]:\boldsymbol{\varepsilon}^{(2)} = \Big[[1-f]\boldsymbol{L}^{(2)} + f\boldsymbol{H}\Big]:\boldsymbol{A}^{(2)}:{}^{\mathrm{M}}\boldsymbol{\varepsilon}\,. \tag{48}$$

Thus, the macroscopic stiffness tensor is given by the expression

$${}^{\mathrm{M}}\boldsymbol{L} = \Big[[1-f]\boldsymbol{L}^{(2)} + f\boldsymbol{H}\Big]:\boldsymbol{A}^{(2)}\,. \tag{49}$$

The properties of the equivalent fiber employed in [66] can be recovered according to

$$\boldsymbol{L}^{\mathrm{eq}} = \boldsymbol{H}:\boldsymbol{T}^{-1}\,. \tag{50}$$

The macroscopic elasticity tensors obtained by our proposed method are formally identical to those given in [108]. The conceptual difference is that instead of seeking the properties of the equivalent fiber, the target is to identify the global strain and stress tensors of the fiber/interface system. For a given macroscopic strain ${}^{\mathrm{M}}\boldsymbol{\varepsilon}$, the average strain and stress in the fiber and matrix read

$$\begin{aligned}
\boldsymbol{\varepsilon}^{(1)} &= \boldsymbol{T}^{(1)}:\boldsymbol{A}^{(2)}:{}^{\mathrm{M}}\boldsymbol{\varepsilon}\,, & \boldsymbol{\sigma}^{(1)} &= \boldsymbol{L}^{(1)}:\boldsymbol{\varepsilon}^{(1)} = \boldsymbol{L}^{(1)}:\boldsymbol{T}^{(1)}:\boldsymbol{A}^{(2)}:{}^{\mathrm{M}}\boldsymbol{\varepsilon}\,,\\
\boldsymbol{\varepsilon}^{(2)} &= \boldsymbol{A}^{(2)}:{}^{\mathrm{M}}\boldsymbol{\varepsilon}\,, & \boldsymbol{\sigma}^{(2)} &= \boldsymbol{L}^{(2)}:\boldsymbol{\varepsilon}^{(2)} = \boldsymbol{L}^{(2)}:\boldsymbol{A}^{(2)}:{}^{\mathrm{M}}\boldsymbol{\varepsilon}\,.
\end{aligned} \tag{51}$$

Using Eq. (46), the average strain and stress on the interface read

$$\widehat{\boldsymbol{\varepsilon}} = f\left[\boldsymbol{T} - \boldsymbol{T}^{(1)}\right] : \boldsymbol{A}^{(2)} : {}^{\mathrm{M}}\boldsymbol{\varepsilon}\,, \qquad \widehat{\boldsymbol{\sigma}} = f\left[\boldsymbol{H} - \boldsymbol{L}^{(1)} : \boldsymbol{T}^{(1)}\right] : \boldsymbol{A}^{(2)} : {}^{\mathrm{M}}\boldsymbol{\varepsilon}\,. \tag{52}$$

So far, the only missing parts to complete the homogenization framework are the interaction tensors $\boldsymbol{T}$, $\boldsymbol{H}$ and $\boldsymbol{T}^{(1)}$. To this end, the extended Eshelby's problem is solved analytically for three boundary value problems similar to those described by Hashin [114] in the composite cylinders assemblage approach. In fiber composites with isotropic or transversely isotropic phases, the strain and stress–strain interaction tensors present transverse isotropy. In Voigt notation, they take the forms

$$\boldsymbol{T} = \begin{bmatrix} T_{11} & T_{11}-T_{44} & T_{13} & 0 & 0 & 0 \\ T_{11}-T_{44} & T_{11} & T_{13} & 0 & 0 & 0 \\ 0 & 0 & 1 & 0 & 0 & 0 \\ 0 & 0 & 0 & T_{44} & 0 & 0 \\ 0 & 0 & 0 & 0 & T_{55} & 0 \\ 0 & 0 & 0 & 0 & 0 & T_{55} \end{bmatrix},$$

$$\boldsymbol{H} = \begin{bmatrix} H_{11} & H_{11}-2H_{44} & H_{13} & 0 & 0 & 0 \\ H_{11}-2H_{44} & H_{11} & H_{13} & 0 & 0 & 0 \\ H_{31} & H_{31} & H_{33} & 0 & 0 & 0 \\ 0 & 0 & 0 & H_{44} & 0 & 0 \\ 0 & 0 & 0 & 0 & H_{55} & 0 \\ 0 & 0 & 0 & 0 & 0 & H_{55} \end{bmatrix}, \tag{53}$$

see [112] for more details on $\boldsymbol{T}$. Note that $\boldsymbol{T}^{(1)}$ has similar structure with $\boldsymbol{T}$. Using this general representation, the three boundary value problems to identify the interaction tensors will be introduced.

*3.3.1.1 Axial shear conditions*For this case, the far field displacement and strain fields applied to the RVE in cylindrical coordinates read

$$\boldsymbol{u}^0_{(r,\theta,z)} = \begin{bmatrix} 0 \\ 0 \\ \beta r\cos\theta \end{bmatrix}, \qquad \boldsymbol{\varepsilon}^0_{(r,\theta,z)} = \begin{bmatrix} 0 & 0 & \frac{\beta}{2}\cos\theta \\ 0 & 0 & -\frac{\beta}{2}\sin\theta \\ \frac{\beta}{2}\cos\theta & -\frac{\beta}{2}\sin\theta & 0 \end{bmatrix}. \tag{54}$$

For these boundary conditions, the important displacements and stresses in the matrix, fiber and interface are given by

$$\begin{aligned} u_z^{(i)}(r,\theta) &= \beta r U_z^{(i)}(r)\cos\theta \text{ with } U_z^{(i)}(r) = \Xi_1^{(i)} + \Xi_2^{(i)}\frac{1}{[r/r_1]^2}\,, \\ \sigma_{rz}^{(i)}(r,\theta) &= \beta\,\Sigma_{rz}^{(i)}(r)\cos\theta \text{ with } \Sigma_{rz}^{(i)}(r) = \mu_{\mathrm{ax}}^{(i)}\left[\Xi_1^{(i)} - \Xi_2^{(i)}\frac{1}{[r/r_1]^2}\right], \\ \overline{\sigma}_{\theta z}(\theta) &= \beta\,\overline{\Sigma}_{\theta z}\sin\theta \qquad \text{with } \overline{\Sigma}_{\theta z} = -\frac{\overline{\mu}_{\mathrm{ax}}}{2}\left[\Xi_1^{(1)} + \Xi_1^{(2)} + \Xi_2^{(1)} + \Xi_2^{(2)}\right], \end{aligned} \tag{55}$$

for $i = 1, 2$ where $i = 1$ corresponds to the fiber and $i = 2$ corresponds to the matrix. The unknowns that need to be defined are $\Xi_1^{(1)}$, $\Xi_2^{(1)}$, $\Xi_1^{(2)}$ and $\Xi_2^{(2)}$. The boundary and interface conditions lead to the following equations

$$\begin{aligned} &u_z^{(1)} \text{ finite at } r = 0 && \rightarrow \Xi_2^{(1)} = 0\,, \\ &\bar{t}_z = \bar{k}_z\,[\![u_z]\!] && \rightarrow \Sigma_{rz}^{(2)}(r_1) + \Sigma_{rz}^{(1)}(r_1) = 2\bar{k}_z r_1\left[U_z^{(2)}(r_1) - U_z^{(1)}(r_1)\right], \\ &\left[\overline{\operatorname{div}\boldsymbol{\sigma}}\right]_z + [\![t_z]\!] = 0 && \rightarrow \frac{1}{r_1}\frac{\partial\overline{\sigma}_{\theta z}(\theta)}{\partial\theta} + \sigma_{rz}^{(2)}(r_1) - \sigma_{rz}^{(1)}(r_1) = 0 \rightarrow \frac{\overline{\Sigma}_{\theta z}}{r_1} + \Sigma_{rz}^{(2)}(r_1) - \Sigma_{rz}^{(1)}(r_1) = 0\,, \\ &u_z^{(2)}(r\rightarrow\infty) = \beta r\cos\theta && \rightarrow \Xi_1^{(2)} = 1\,. \end{aligned} \tag{56}$$

Solving the above linear system, the average strain and stress in the fiber/interface system read

$$\langle \boldsymbol{\varepsilon} \rangle^{-}_{\Omega_1} = U_z^{(1)}(r_1)\, \boldsymbol{\varepsilon}^0\,, \qquad \langle \boldsymbol{\varepsilon} \rangle^{+}_{\Omega_1} = U_z^{(2)}(r_1)\, \boldsymbol{\varepsilon}^0\,, \qquad \langle \boldsymbol{\sigma} \rangle^{+}_{\Omega_1} = \Sigma_{rz}^{(2)}(r_1)\, \boldsymbol{\varepsilon}^0. \tag{57}$$

Since $\boldsymbol{H}$ is a stress-type tensor and the applied shear angle is β, the term H_{55} must be equal to the generated stress on the fiber/interface system. Consequently, the axial shear interaction terms are

$$T_{55}^{(1)} = \Xi_1^{(1)}\,, \qquad T_{55} = 1 + \Xi_2^{(2)}\,, \qquad H_{55} = \mu_{\text{ax}}^{(2)} \left[1 - \Xi_2^{(2)}\right]. \tag{58}$$

*3.3.1.2 Transverse shear conditions*For this case, the far field displacement and strain fields applied to the RVE in the cylindrical coordinates read

$$\boldsymbol{u}^0_{(r,\theta,z)} = \begin{bmatrix} \beta r \sin 2\theta \\ \beta r \cos 2\theta \\ 0 \end{bmatrix}, \qquad \boldsymbol{\varepsilon}^0_{(r,\theta,z)} = \begin{bmatrix} \beta \sin 2\theta & \beta \cos 2\theta & 0 \\ \beta \cos 2\theta & -\beta \sin 2\theta & 0 \\ 0 & 0 & 0 \end{bmatrix}. \tag{59}$$

For these boundary conditions, the important displacements and stresses at each phase are given by the general expressions

$$\begin{aligned}
&u_r^{(i)}(r,\theta) = \beta\, r\, U_r^{(i)}(r)\, \sin 2\theta \qquad \text{with} \quad U_r^{(i)}(r) = \frac{\kappa_{\text{tr}}^{(i)} - \mu_{\text{tr}}^{(i)}}{2\kappa_{\text{tr}}^{(i)} + \mu_{\text{tr}}^{(i)}} [r/r_1]^2 \Xi_1^{(i)} + \Xi_2^{(i)} \\
&- \frac{1}{[r/r_1]^4}\Xi_3^{(i)} + \frac{\kappa_{\text{tr}}^{(i)} + \mu_{\text{tr}}^{(i)}}{\mu_{\text{tr}}^{(i)}} \frac{1}{[r/r_1]^2}\Xi_4^{(i)}\,, \\
&u_\theta^{(i)}(r,\theta) = \beta\, r\, U_\theta^{(i)}(r)\, \cos 2\theta \qquad \text{with} \quad U_\theta^{(i)}(r) = [r/r_1]^2 \Xi_1^{(i)} + \Xi_2^{(i)} + \frac{1}{[r/r_1]^4}\Xi_3^{(i)} + \frac{1}{[r/r_1]^2}\Xi_4^{(i)}\,, \\
&\sigma_{rr}^{(i)}(r,\theta) = \beta\, \Sigma_{rr}^{(i)}(r)\, \sin 2\theta \qquad \text{with} \quad \Sigma_{rr}^{(i)}(r) = 2\mu_{\text{tr}}^{(i)} \Xi_2^{(i)} + 6\mu_{\text{tr}}^{(i)} \frac{1}{[r/r_1]^4}\Xi_3^{(i)} - 4\kappa_{\text{tr}}^{(i)} \frac{1}{[r/r_1]^2}\Xi_4^{(i)}\,, \\
&\sigma_{r\theta}^{(i)}(r,\theta) = \beta\, \Sigma_{r\theta}^{(i)}(r)\, \cos 2\theta \qquad \text{with} \quad \Sigma_{r\theta}^{(i)}(r) = \frac{6\kappa_{\text{tr}}^{(i)} \mu_{\text{tr}}^{(i)}}{2\kappa_{\text{tr}}^{(i)} + \mu_{\text{tr}}^{(i)}} [r/r_1]^2 \Xi_1^{(i)} + 2\mu_{\text{tr}}^{(i)} \Xi_2^{(i)} \\
&- 6\mu_{\text{tr}}^{(i)} \frac{1}{[r/r_1]^4}\Xi_3^{(i)} + 2\kappa_{\text{tr}}^{(i)} \frac{1}{[r/r_1]^2}\Xi_4^{(i)}\,, \\
&\overline{u}_r(\theta) = \beta\, r_1\, \overline{U}_r\, \sin 2\theta \qquad \text{with} \quad \overline{U}_r = \frac{U_r^{(1)}(r_1) + U_r^{(2)}(r_1)}{2}\,, \\
&\overline{u}_\theta(\theta) = \beta\, r_1\, \overline{U}_\theta\, \cos 2\theta \qquad \text{with} \quad \overline{U}_\theta = \frac{U_\theta^{(1)}(r_1) + U_\theta^{(2)}(r_1)}{2}\,, \\
&\overline{\sigma}_{\theta\theta}(\theta) = \beta\, \overline{\Sigma}_{\theta\theta}\, \sin 2\theta \qquad \text{with} \quad \overline{\Sigma}_{\theta\theta} = \overline{m}\left[\overline{U}_r - 2\overline{U}_\theta\right],
\end{aligned} \tag{60}$$

for $i = 1, 2$ where $i = 1$ corresponds to the fiber and $i = 2$ corresponds to the matrix. The unknowns that need to be defined are $\Xi_1^{(1)}$, $\Xi_2^{(1)}$, $\Xi_3^{(1)}$, $\Xi_4^{(1)}$, $\Xi_1^{(2)}$, $\Xi_2^{(2)}$, $\Xi_3^{(2)}$ and $\Xi_4^{(2)}$. The boundary and interface conditions necessitate the following equations

$$\begin{aligned}
&u_r^{(1)}, u_\theta^{(1)} \text{ finite at } r = 0 \qquad \rightarrow \quad \Xi_3^{(1)} = \Xi_4^{(1)} = 0\,, \\
&\bar{t}_r = \bar{k}_r [\![u_r]\!] \qquad \rightarrow \quad \Sigma_{rr}^{(2)}(r_1) + \Sigma_{rr}^{(1)}(r_1) = 2\bar{k}_r r_1 \left[U_r^{(2)}(r_1) - U_r^{(1)}(r_1)\right], \\
&\bar{t}_\theta = \bar{k}_\theta [\![u_\theta]\!] \qquad \rightarrow \quad \Sigma_{r\theta}^{(2)}(r_1) + \Sigma_{r\theta}^{(1)}(r_1) = 2\bar{k}_\theta r_1 \left[U_\theta^{(2)}(r_1) - U_\theta^{(1)}(r_1)\right], \\
&\left[\overline{\text{div}\,\sigma}\right]_r + [\![t_r]\!] = 0 \qquad \rightarrow \quad -\frac{\overline{\sigma}_{\theta\theta}(\theta)}{r_1} + \sigma_{rr}^{(2)}(r_1) - \sigma_{rr}^{(1)}(r_1) = 0 \rightarrow -\frac{\overline{\Sigma}_{\theta\theta}}{r_1} + \Sigma_{rr}^{(2)}(r_1) - \Sigma_{rr}^{(1)}(r_1) = 0\,, \\
&\left[\overline{\text{div}\,\sigma}\right]_\theta + [\![t_\theta]\!] = 0 \qquad \rightarrow \quad \frac{1}{r_1}\frac{\partial \overline{\sigma}_{\theta\theta}(\theta)}{\partial \theta} + \sigma_{r\theta}^{(2)}(r_1) - \sigma_{r\theta}^{(1)}(r_1) = 0 \rightarrow \frac{2\,\overline{\Sigma}_{\theta\theta}}{r_1} + \Sigma_{r\theta}^{(2)}(r_1) - \Sigma_{r\theta}^{(1)}(r_1) = 0\,, \\
&u_r^{(2)}(r \rightarrow \infty) = \beta r \sin 2\theta \quad \text{and} \quad u_\theta^{(2)}(r \rightarrow \infty) = \beta r \cos 2\theta \quad \rightarrow \quad \Xi_1^{(2)} = 0 \quad \text{and} \quad \Xi_2^{(2)} = 1\,.
\end{aligned} \tag{61}$$

Solving the above linear system, the average strain and stress in the fiber/interface system are

$$\langle\boldsymbol{\varepsilon}\rangle^{-}_{\Omega_1} = \frac{1}{2}\left[U_r^{(1)}(r_1) + U_\theta^{(1)}(r_1)\right]\boldsymbol{\varepsilon}^0\,, \quad \langle\boldsymbol{\varepsilon}\rangle^{+}_{\Omega_1} = \frac{1}{2}\left[U_r^{(2)}(r_1) + U_\theta^{(2)}(r_1)\right]\boldsymbol{\varepsilon}^0\,,$$
$$\langle\boldsymbol{\sigma}\rangle^{+}_{\Omega_1} = \frac{1}{2}\left[\Sigma_{rr}^{(2)}(r_1) + \Sigma_{r\theta}^{(2)}(r_1)\right]\boldsymbol{\varepsilon}^0\,. \tag{62}$$

Again, since $\boldsymbol{H}$ is a stress-type tensor and the applied shear angle is 2β, the term H_{44} must be equal to the half of the generated stress on the fiber/interface system. Consequently, the transverse shear interaction terms are

$$T_{44}^{(1)} = \frac{3\kappa_{\text{tr}}^{(1)}}{4\kappa_{\text{tr}}^{(1)} + 2\mu_{\text{tr}}^{(1)}}\Xi_1^{(1)} + \Xi_2^{(1)}\,, \qquad T_{44} = 1 + \frac{\kappa_{\text{tr}}^{(2)} + 2\mu_{\text{tr}}^{(2)}}{2\mu_{\text{tr}}^{(2)}}\Xi_4^{(2)}\,,$$
$$H_{44} = \mu_{\text{tr}}^{(2)} - \frac{\kappa_{\text{tr}}^{(2)}}{2}\Xi_4^{(2)}\,. \tag{63}$$

*3.3.1.3 Axisymmetric conditions*For this case, the far field displacement and strain fields applied to the RVE in the cylindrical coordinates read

$$\boldsymbol{u}^0_{(r,\theta,z)} = \begin{bmatrix} e^T r \\ 0 \\ e^A z \end{bmatrix}, \qquad \boldsymbol{\varepsilon}^0_{(r,\theta,z)} = \begin{bmatrix} e^T & 0 & 0 \\ 0 & e^T & 0 \\ 0 & 0 & e^A \end{bmatrix}. \tag{64}$$

For these boundary conditions, the important displacements and stresses in the matrix, fiber and the interface are given by

$$\begin{aligned}
&u_z^{(i)}(z) = e^A z\,,\\
&u_r^{(i)}(r) = e^T r U_r^{(i)}(r) && \text{with } U_r^{(i)}(r) = \left[\Xi_1^{(i)} + \Xi_2^{(i)}\frac{1}{[r/r_1]^2}\right],\\
&\sigma_{rr}^{(i)}(r) = e^T \Sigma_{rr}^{(i)}(r) + e^A l^{(i)} && \text{with } \Sigma_{rr}^{(i)}(r) = 2\kappa_{\text{tr}}^{(i)}\Xi_1^{(i)} - 2\mu_{\text{tr}}^{(i)}\Xi_2^{(i)}\frac{1}{[r/r_1]^2}\,,\\
&\sigma_{zz}^{(i)} = e^T \Sigma_{zz}^{(i)} + e^A n^{(i)} && \text{with } \Sigma_{zz}^{(i)} = 2l^{(i)}\Xi_1^{(i)}\,,\\
&\overline{\sigma}_{\theta\theta} = e^T\ \overline{\Sigma}_{\theta\theta} + e^A\overline{l} && \text{with } \overline{\Sigma}_{\theta\theta} = \frac{\overline{m}}{2}\left[\Xi_1^{(1)} + \Xi_1^{(2)} + \Xi_2^{(1)} + \Xi_2^{(2)}\right],\\
&\overline{\sigma}_{zz} = e^T\ \overline{\Sigma}_{zz} + e^A\overline{n} && \text{with } \overline{\Sigma}_{zz} = \frac{\overline{l}}{2}\left[\Xi_1^{(1)} + \Xi_1^{(2)} + \Xi_2^{(1)} + \Xi_2^{(2)}\right],
\end{aligned} \tag{65}$$

for $i = 1, 2$ where $i = 1$ corresponds to the fiber and $i = 2$ corresponds to the matrix. The unknowns that need to be defined are $\Xi_1^{(1)}$, $\Xi_2^{(1)}$, $\Xi_1^{(2)}$ and $\Xi_2^{(2)}$. The boundary and interface conditions necessitate

$$\begin{aligned}
&u_r^{(1)} \text{ finite at } r = 0 && \rightarrow\ \Xi_2^{(1)} = 0\,,\\
&\bar{t}_r = \bar{k}_r\,[\![u_r]\!] && \rightarrow\ \sigma_{rr}^{(2)}(r_1) + \sigma_{rr}^{(1)}(r_1) = 2\bar{k}_r\left[u_r^{(2)}(r_1) - u_r^{(1)}(r_1)\right],\\
&\left[\overline{\text{div}}\,\overline{\boldsymbol{\sigma}}\right]_r + [\![t_r]\!] = 0 && \rightarrow\ -\frac{\overline{\sigma}_{\theta\theta}}{r_1} + \sigma_{rr}^{(2)}(r_1) - \sigma_{rr}^{(1)}(r_1) = 0\,,\\
&u_r^{(2)}(r\to\infty) = e^T r && \rightarrow\ \Xi_1^{(2)} = 1\,.
\end{aligned} \tag{66}$$

Solving the above linear system, the average strain and stress in the fiber/interface system are

$$\begin{aligned}
\langle\boldsymbol{\varepsilon}\rangle^{-}_{\Omega_1} &= \begin{bmatrix} U_r^{(1)}(r_1)\,e^T & 0 & 0 \\ 0 & U_r^{(1)}(r_1)\,e^T & 0 \\ 0 & 0 & e^A \end{bmatrix}, \quad \langle\boldsymbol{\varepsilon}\rangle^{+}_{\Omega_1} = \begin{bmatrix} U_r^{(2)}(r_1)\,e^T & 0 & 0 \\ 0 & U_r^{(2)}(r_1)\,e^T & 0 \\ 0 & 0 & e^A \end{bmatrix},\\
\langle\boldsymbol{\sigma}\rangle^{+}_{\Omega_1} &= \begin{bmatrix} \Sigma_{rr}^{(2)}(r_1) & 0 & 0 \\ 0 & \Sigma_{rr}^{(2)}(r_1) & 0 \\ 0 & 0 & \Sigma_{zz}^{(1)} + \dfrac{2\overline{\Sigma}_{zz}}{r_1} \end{bmatrix} e^T + \begin{bmatrix} l^{(2)} & 0 & 0 \\ 0 & l^{(2)} & 0 \\ 0 & 0 & n^{(1)} + \dfrac{2\overline{n}}{r_1} \end{bmatrix} e^A\,.
\end{aligned} \tag{67}$$

At this stage, two cases are examined:

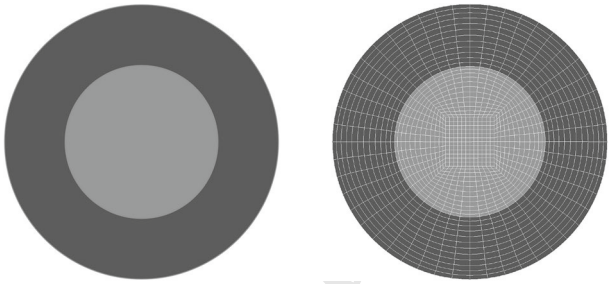

Fig. 8 Mesh quality of the RVE for finite element analysis. The domain is discretized using biquadratic Lagrange elements

- $e^A = 0$ and $e^T = 1$: The constants from the solution of the linear system are denoted as $\Xi_{11}^{(1)}$ and $\Xi_{21}^{(2)}$. For this condition, the general forms of the dilute concentration tensors in Eq. (53) permit to write

$$\begin{aligned} \langle \varepsilon_{xx} \rangle_{\Omega_1}^{-} &= T_{11}^{(1)} + [T_{11}^{(1)} - T_{44}^{(1)}] , & \langle \varepsilon_{xx} \rangle_{\Omega_1}^{+} &= T_{11} + [T_{11} - T_{44}] , \\ \langle \sigma_{xx} \rangle_{\Omega_1}^{+} &= H_{11} + [H_{11} - 2H_{44}] , & \langle \sigma_{zz} \rangle_{\Omega_1}^{+} &= 2H_{31} . \end{aligned} \tag{68}$$

From (67), clearly we have

$$\begin{aligned} T_{11}^{(1)} &= \frac{1}{2}\left[\Xi_{11}^{(1)} + T_{44}^{(1)}\right] , & T_{11} &= \frac{1}{2}\left[1 + \Xi_{21}^{(2)} + T_{44}\right] , \\ H_{11} &= \kappa_{\mathrm{tr}}^{(2)} - \mu_{\mathrm{tr}}^{(2)}\Xi_{21}^{(2)} + H_{44} , & H_{31} &= l^{(1)}\Xi_{11}^{(1)} + \frac{\bar{l}}{2r_1}\left[1 + \Xi_{11}^{(1)} + \Xi_{21}^{(2)}\right] . \end{aligned} \tag{69}$$

- $e^A = e^T = 1$: The constants from the solution of the linear system are denoted as $\Xi_{12}^{(1)}$ and $\Xi_{22}^{(2)}$. For this condition, the general forms of the dilute concentration tensors in Eq. (53) permit to write

$$\begin{aligned} \langle \varepsilon_{xx} \rangle_{\Omega_1}^{-} &= T_{11}^{(1)} + \left[T_{11}^{(1)} - T_{44}^{(1)}\right] + T_{13}^{(1)} , & \langle \varepsilon_{xx} \rangle_{\Omega_1}^{+} &= T_{11} + \left[T_{11} - T_{44}\right] + T_{13} , \\ \langle \sigma_{xx} \rangle_{\Omega_1}^{+} &= H_{11} + \left[H_{11} - 2H_{44}\right] + H_{13} , & \langle \sigma_{zz} \rangle_{\Omega_1}^{+} &= 2H_{31} + H_{33} . \end{aligned} \tag{70}$$

Combining the last expression with (67) and (69) yields

$$\begin{aligned} T_{13}^{(1)} &= \Xi_{12}^{(1)} + T_{44}^{(1)} - 2T_{11}^{(1)} , \\ T_{13} &= 1 + \Xi_{22}^{(2)} + T_{44} - 2T_{11} , \\ H_{13} &= 2\kappa_{\mathrm{tr}}^{(2)} - 2\mu_{\mathrm{tr}}^{(2)}\Xi_{22}^{(2)} + l^{(2)} + 2H_{44} - 2H_{11} , \\ H_{33} &= 2l^{(1)}\Xi_{12}^{(1)} + \frac{\bar{l}}{r_1}\left[1 + \Xi_{12}^{(1)} + \Xi_{22}^{(2)}\right] + n^{(1)} + \frac{2\bar{n}}{r_1} - 2H_{31} . \end{aligned} \tag{71}$$

Expressions (58), (63), (69) and (71) provide all the required coefficients for the interaction tensors, which in turn can be implemented in the Mori–Tanaka scheme to identify the macroscopic elasticity tensor of fiber composites. The components of ${}^{\mathrm{M}}\boldsymbol{L}$ are expressed as given in Eq. (10).

4 Numerical results

The goal of this section is to evaluate the performance of the proposed analytical solutions through a series of numerical examples. In doing so, the influence of the general interfaces on the overall material response is investigated and compared against computational simulations using the finite element method elaborated in [91]. The computational analysis is carried out using our in-house finite element code applied to the RVE discretized by biquadratic Lagrange elements as shown in Fig. 8. For all examples, the solution procedures are robust and show asymptotically the quadratic rate of convergence associated with the Newton–Raphson scheme. For all the cases, the volume fraction $f = 30\%$ is assumed. The RVE size varies from 0.001 to 1000, and three different stiffness ratios of 0.1, 1 and 10 are studied. The stiffness ratio denoted as incl./matr. is the

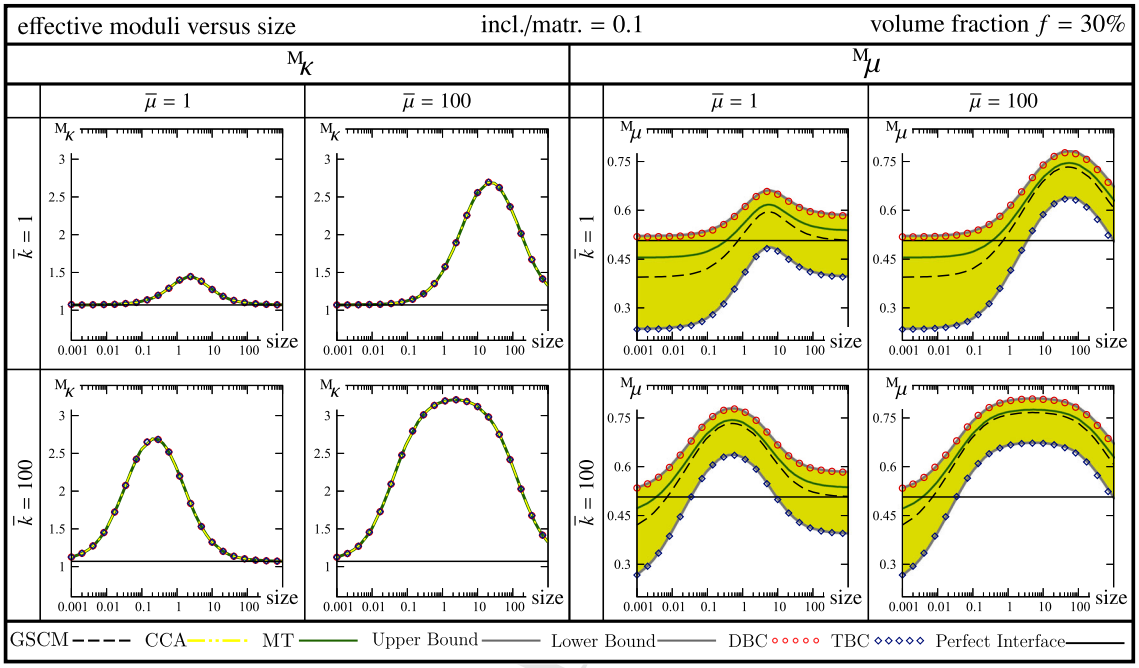

Fig. 9 The effective bulk and shear moduli versus size for incl./matr. = 0.1. The lines correspond to the analytical solutions, and dots correspond to the numerical results using the finite element method. "CCA" and "GSCM" indicate the effective properties obtained via the solution proposed in Sects. 3.2.1 and 3.2.2. "Upper Bound" and "Lower Bound" refer to our proposed bounds in Sects. 3.2.3 and 3.2.4. "MT" corresponds to our proposed solution in Sect. 3.3

ratio of the inclusion to matrix Lamé parameters. The stiffness ratio 0.1 corresponds to a matrix 10 times stiffer than the inclusion and in the limit of incl./matr. $\to$ 0, the inclusion resembles a void. The stiffness ratio 10 corresponds to an inclusion 10 times stiffer than the matrix and in the limit of incl./matr. $\to \infty$, the inclusion acts as being rigid. Clearly, the stiffness ratio 1 represents identical inclusion and matrix. Throughout the numerical examples, the matrix Lamé parameters are $\lambda_2 = \mu_2 = 1$ and the inclusion Lamé parameters vary in accordance with the prescribed stiffness ratios. The interface in-plane resistance $\overline{\mu}$ corresponds to the resistance of the interface against stretch and is set to $\overline{\mu} = 1$ indicating a low in-plane resistance and $\overline{\mu} = 100$ indicating a very high resistance. On the other hand, the two considered values for the orthogonal interface resistance are $\overline{k} = 1$ indicating a low opening resistance and $\overline{k} = 100$ indicating a high opening resistance. In the limit $\overline{k} \to \infty$, the interface remains coherent and does not allow for opening. On the contrary, $\overline{k} \to 0$ indicates no orthogonal resistance and the fiber behaves entirely detached from the matrix. It shall be emphasized that depending on the choice of the general interface parameters any of the perfect, elastic or cohesive interface models could be recovered, as shown in Fig. 1. The conditions $\overline{\mu} \neq 0$ and $\overline{k} \to \infty$ recover the elastic interface model. The cohesive interface is recovered when $\overline{\mu} = 0$ and $\overline{k} \nrightarrow \infty$. Finally, the perfect interface model is recovered when $\overline{\mu} = 0$ and $\overline{k} \to \infty$.

Figures 9, 10 and 11 illustrate the effective bulk modulus $^{M}\kappa$ and shear modulus $^{M}\mu$ versus size for different stiffness ratios. Each column corresponds to a specific in-plane resistance $\overline{\mu}$, and each row corresponds to a specific orthogonal resistance $\overline{k}$. The solid straight black line shows the effective response due to the perfect interface. Lines indicate the analytical solutions corresponding to the analytical approaches developed in Sects. 3.2.1 and 3.3. Red circular points and blue rectangular points correspond to computational results using the finite element method obtained via prescribing DBC and TBC, respectively.

A remarkable agreement between the analytical solutions and the computational results are consistently observed for all the examples. For all the cases, a size-dependent response is observed due to the presence of the general interface. For the bulk modulus, all the solutions render a consistent behavior with respect to the perfect interface solution. The results coincide with the perfect interface solution at small sizes. Increasing the size results in deviation from the perfect interface solution until a critical size at which an extremum is reached. Further increase in size yields asymptotic convergence of the results to the perfect interface solution which is due to the diminished interface effects at large sizes. For incl./matr. = 0.1, the results corresponding

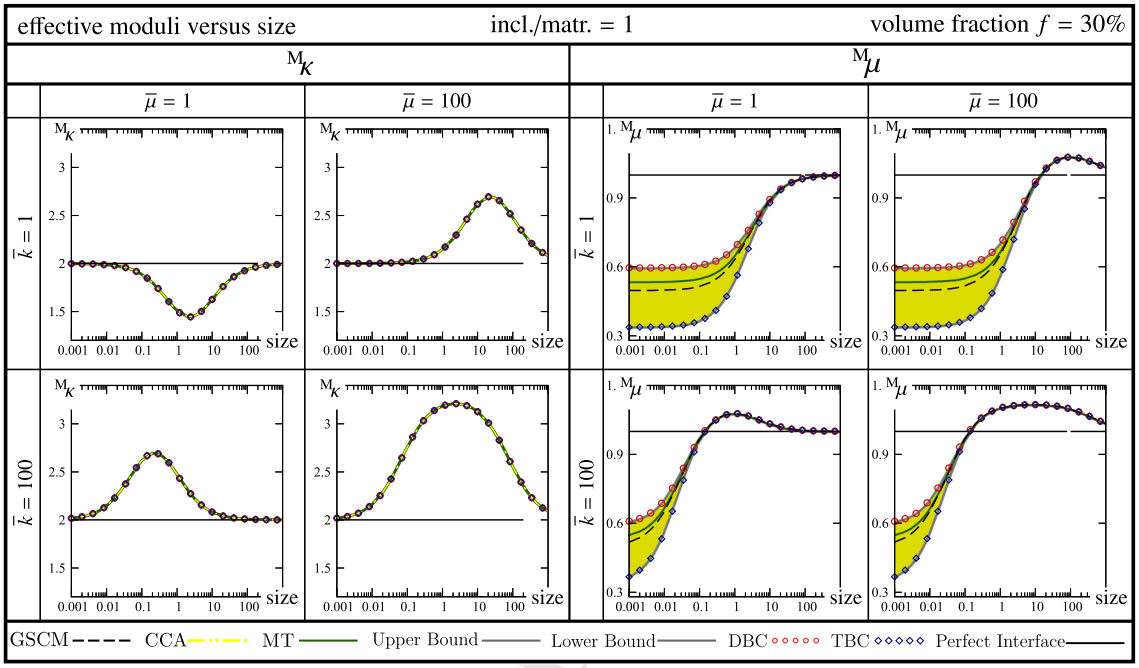

Fig. 10 The effective bulk and shear moduli versus size for incl./matr. = 1. The lines correspond to the analytical solutions, and dots correspond to the numerical results using the finite element method. "CCA" and "GSCM" indicate the effective properties obtained via the solution proposed in Sects. 3.2.1 and 3.2.2 . "Upper Bound" and "Lower Bound" refer to our proposed bounds in Sects. 3.2.3 and 3.2.4 . "MT" corresponds to our proposed solution in Sect. 3.3.

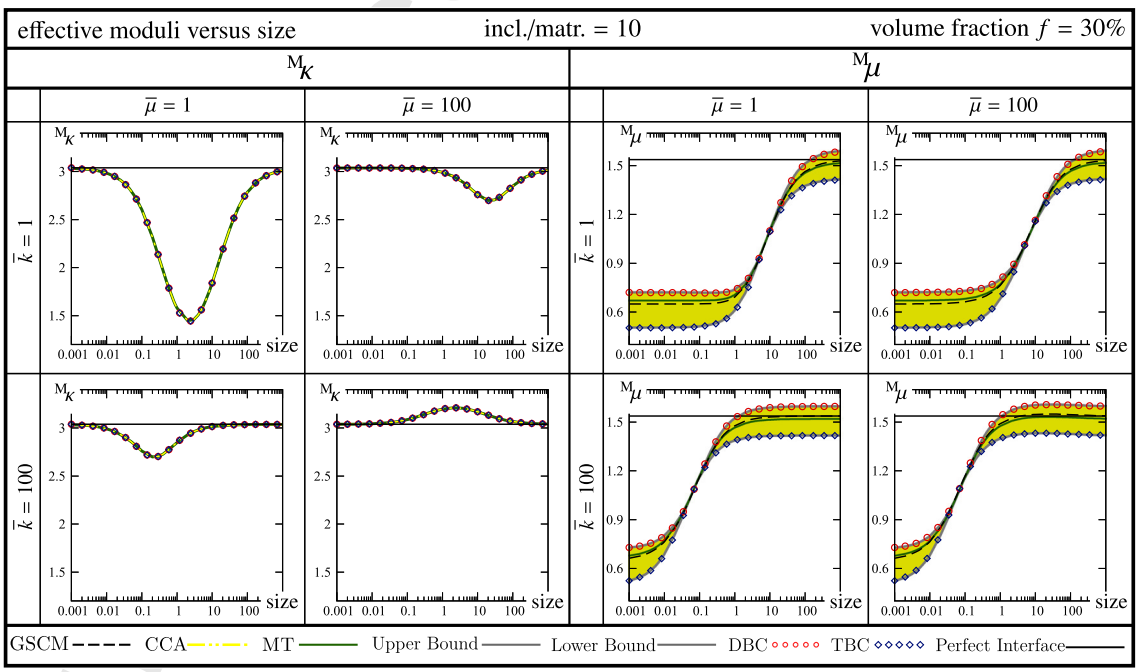

Fig. 11 The effective bulk and shear moduli versus size for incl./matr. = 10. The lines correspond to the analytical solutions, and dots correspond to the numerical results using the finite element method. "CCA" and "GSCM" indicate the effective properties obtained via the solution proposed in Sects. 3.2.1 and 3.2.2 . "Upper Bound" and "Lower Bound" refer to our proposed bounds in Sects. 3.2.3 and 3.2.4 . "MT" corresponds to our proposed solution in Sect. 3.3

to general interface always overestimate to those obtained from the perfect interface model. However, for the other stiffness ratios, depending on the interface parameters, the results render either a weaker or a stronger response compared to the perfect interface solution. Evidently, if the interface parameters are taken enough large, the response due to the general interface is stiffer than those of the perfect interface. Overall, an important observation and especially useful for computational material design is that in the presence of interfaces, even if the inclusion is identical to the matrix, various combinations of parameters could result in substantially different but also size-dependent overall material behavior. For the shear modulus, there is perfect agreement between the upper bound and DBC and the lower bound and TBC. When incl./matr. $= 0.1$, the bounds never coincide. When incl./matr. $= 1$ in Fig. 10, the upper and the lower bounds *converge* at larger sizes since incl./matr. $= 1$ implies identical matrix and inclusion and hence, identical responses are seen when the interface effects become negligible enough at large sizes. For incl./matr. $= 10$, the bounds tend to approach to each other until they coincide at a specific sizes and then they distant from each other as size increases. A particular significant observation is that the generalized self-consistent method and the modified Mori–Tanaka method do not provide similar estimates for the effective shear modulus. For incl./matr. $= 0.1$ and incl./matr. $= 1$, the response obtained from GSCM underestimates that of MT method. However, when incl./matr. $= 10$, the results corresponding to GSCM underestimate the ones obtained from MT before the bounds coincide, whereas the opposite story holds after the bounds coincidence.

Remark In view of the behavior of the effective bulk modulus ${}^{\mathrm{M}}\kappa$, it is observed that the general interface model at both limits of small and large sizes converges to the perfect interface model. The interface effect is decreasing when increasing the size, and thus, its behavior at large sizes is fairly obvious. At small scales, however, further discussion is required to justify the influence of the interface on the overall material response. The effective behavior of the general interface model can be explained by the fact that it combines the two opposing cohesive and elastic interface models, schematically illustrated in Fig. 1. The elastic interface model results in a *smaller-stronger* effect in contrast to the *smaller-weaker* effect of the cohesive interface model. At large sizes, neither of the interface effects is present. But at small sizes, both of the interface effects are present and eventually cancel each other. Furthermore, we can elaborate on this observation from an analytical perspective. To do so, we re-express the effective bulk modulus (25) as

$$
{}^{\mathrm{M}}\kappa = \lambda_2 + \mu_2 + \frac{f}{\dfrac{1}{\dfrac{\Big[\lambda_1+\mu_1\Big]\Big[4\overline{k}r_1^3+2\overline{\mu}r_1\Big]+4\overline{k}\overline{\mu}r_1^2}{4r_1^2\Big[2\lambda_1+2\mu_1+\overline{k}r_1\Big]+2\overline{\mu}r_1}-\Big[\lambda_2+\mu_2\Big]}+\dfrac{1-f}{\lambda_2+2\mu_2}},
$$

thereby gaining a better insight on ${}^{\mathrm{M}}\kappa$ in terms of r_1. This relation in both limits simplifies to

$$
r\to 0 \quad \text{or} \quad r\to\infty \qquad \Rightarrow \qquad {}^{\mathrm{M}}\kappa = \lambda_2+\mu_2+\frac{f}{\dfrac{1}{[\lambda_1+\mu_1]-[\lambda_2+\mu_2]}+\dfrac{1-f}{\lambda_2+2\mu_2}} \tag{72}
$$

which corresponds exactly to the solution associated with the perfect interface model.

Inspired by the observations made throughout the numerical examples, it is possible to distinguish between two dissimilar bounds on the overall behavior of the microstructure, namely *size-dependent bounds* and *ultimate bounds*. Size-dependent bounds are the bounds on the effective behavior of the microstructure at any given size. The upper and lower size-dependent bounds correspond to the solution of the boundary value problem associated with DBC and TBC, respectively. On the other hand, we also observe that the macroscopic response is always bounded between two specific values regardless of the size of the microstructure and thus, we refer to them as ultimate bounds. In the case of a stiff inclusion within a more compliant matrix such as incl./matr. $= 10$ shown in Fig. 11, the ultimate bounds are reached at extreme sizes. However, the ultimate bounds may be reached at critical sizes and not necessarily at the limits, see, for instance, Fig. 9. In fact, Fig. 12 elucidates the notions of ultimate and size-dependent bounds schematically. Size-dependent bounds are local in the sense that for a specific interface and material parameters, they vary with respect to size. In contrast, the ultimate bounds are independent of size and they entirely depend on the interface and bulk material properties. As pointed out earlier, the size-dependent bounds coincide in the case of the effective bulk modulus ${}^{\mathrm{M}}\kappa$ and are only distinct in the case of the effective shear modulus ${}^{\mathrm{M}}\mu$. One can mention that this conclusion for general interface is in agreement with that derived by Hashin and Rosen for the case of a perfect interface [107].

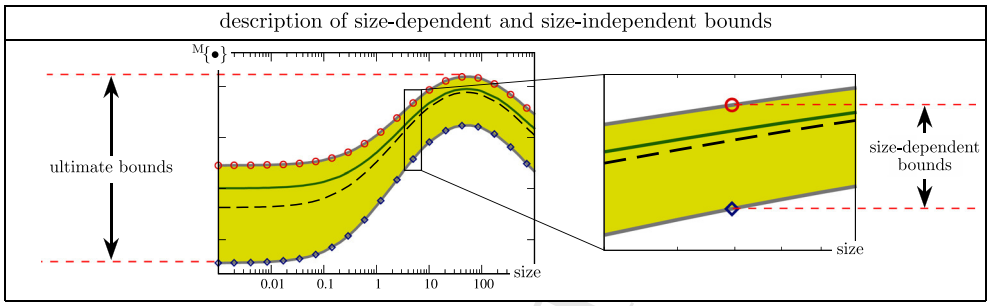

Fig. 12 Schematic illustration of size-dependent and ultimate bounds. The size-dependent bounds are the bounds on the effective behavior of the microstructure at any given size. The ultimate bounds are independent of size, and they entirely depend on the interface and bulk material properties

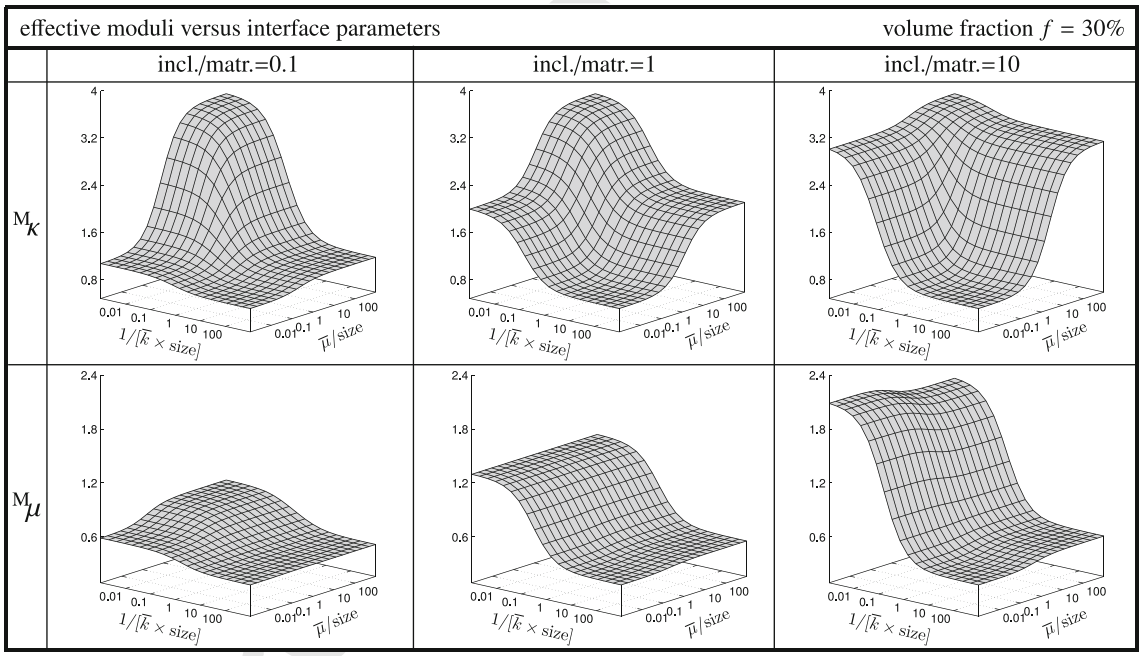

Fig. 13 Effective moduli versus dimensionless interface parameters

To pinpoint the effects of the interface parameters on the overall material response of composites with general interfaces, Fig. 13 illustrates the variation of the effective moduli versus interface parameters. Each column corresponds to a specific stiffness ratio. The top row corresponds to effective bulk modulus $^{M}\kappa$, and the bottom row corresponds to the effective shear modulus $^{M}\mu$. Note that the interface orthogonal resistance $\overline{k}$ has the inverse length dimension and thus multiplied to the size to become dimensionless. On the other hand, the interface elastic parameter $\overline{\mu}$ has the length dimension and thus divided by the size to become dimensionless. For the effective bulk modulus, increasing any of the interface parameters results in stiffer material response. For two extreme cases of very strong and very weak interfaces, the associated overall response is similar for all stiffness ratios. On the other hand, for the shear modulus, when incl./matr. $= 0.1$, increasing the interface parameters stiffens the response. For incl./matr. $= 1$, the overall response shows no sensitivity to $\overline{\mu}$, whereas increasing $\overline{k}$ yields stronger response. An interesting observation arises for incl./matr. $= 10$ where increasing $\overline{k}$ results in stiffer response but increasing $\overline{\mu}$ might lead to either softer or stiffer response depending on the size.

Figures 14 and 15 illustrate the stress distribution within the microstructure at different sizes and for different stiffness ratios. More precisely, the color patterns display $[\boldsymbol{\sigma}_{xx} + \boldsymbol{\sigma}_{yy}]/2$ in Fig. 14 and $[\boldsymbol{\sigma}]_{xy}$ in Fig. 15. This choice is made to provide meaningful stress distributions for each case. In the case of Fig. 14, volumetric expansion is prescribed on the RVE to compute the effective bulk modulus $^{M}\kappa$ and thus, a pressure-

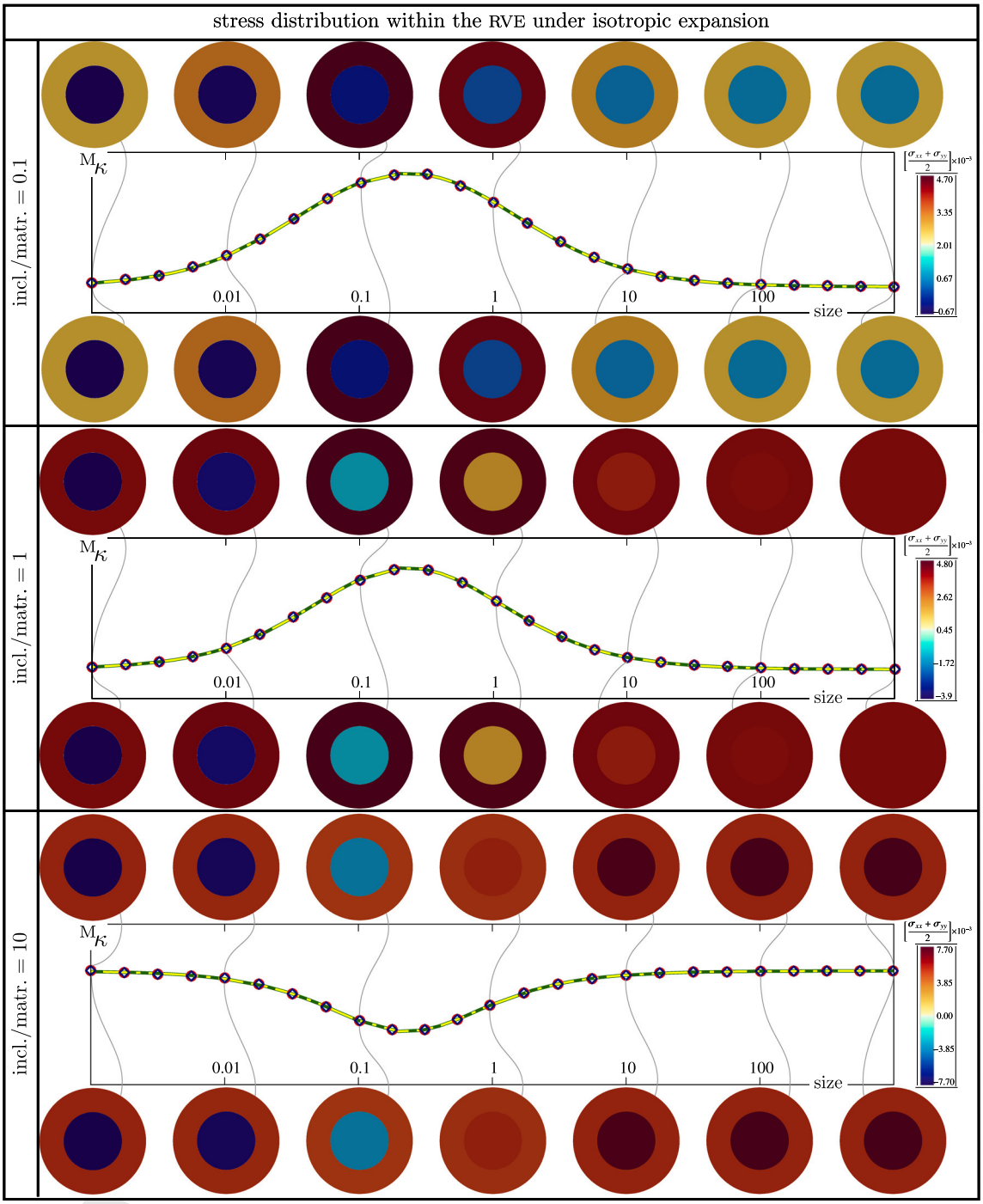

Fig. 14 Illustration of the stress distribution within the microstructure due to isotropic expansion at different sizes and for different stiffness ratios. The upper row of stress distributions on each graph correspond to DBC and the lower row to TBC

like quantity $[\boldsymbol{\sigma}_{xx}+\boldsymbol{\sigma}_{yy}]/2$ is more relevant and informative. On the other hand, in the case of Fig. 15, a simple shear is prescribed on the RVE to compute the effective shear modulus ${}^{\mathrm{M}}\mu$ in which case the shear component of the stress $[\boldsymbol{\sigma}]_{xy}$ is a more appropriate quantity to look at. Obviously, for the sake of a better presentation, all the RVEs are scaled to the same size. On each graph, the upper row and lower row show the stress distributions corresponding to DBC and TBC, respectively. Both figures compare the cases with the interface parameters $\overline{k}=100$ and $\overline{\mu}=1$ from Figs. 9, 10 and 11. For the expansion case in Fig. 14, the stress patterns due to DBC

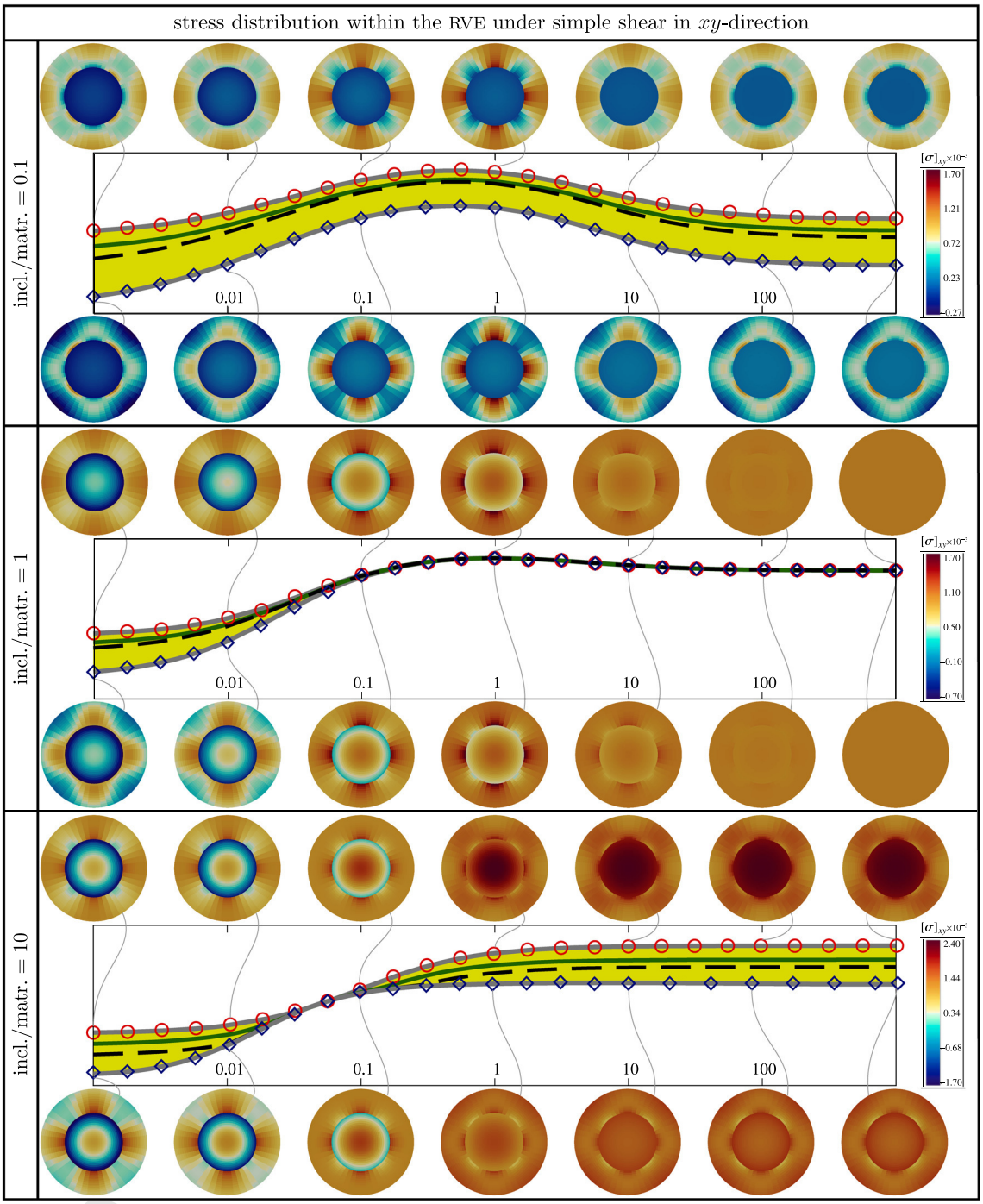

Fig. 15 Illustration of the stress distribution within the microstructure due to simple shear at different sizes and for different stiffness ratios. The upper row of stress distributions on each graph corresponds to DBC, and the lower row to TBC

and TBC are identical, and thus, the effective bulk modulus ${}^{\mathrm{M}}\kappa$ is same, at any given size. But that is not the case for the effective shear modulus. For the non-coinciding cases, the stress due to DBC always overestimates the stress due to TBC and hence stiffer overall response. For the coinciding cases, the stresses due to DBC and TBC are identical which justifies the same overall response. Moreover, for incl./matr. $= 0.1$, the stress in the fiber is less than the matrix at any size. For incl./matr. $= 1$, the same story holds at small sizes, whereas at large size, the stresses become similar since interface effects become negligible and the bulk materials are

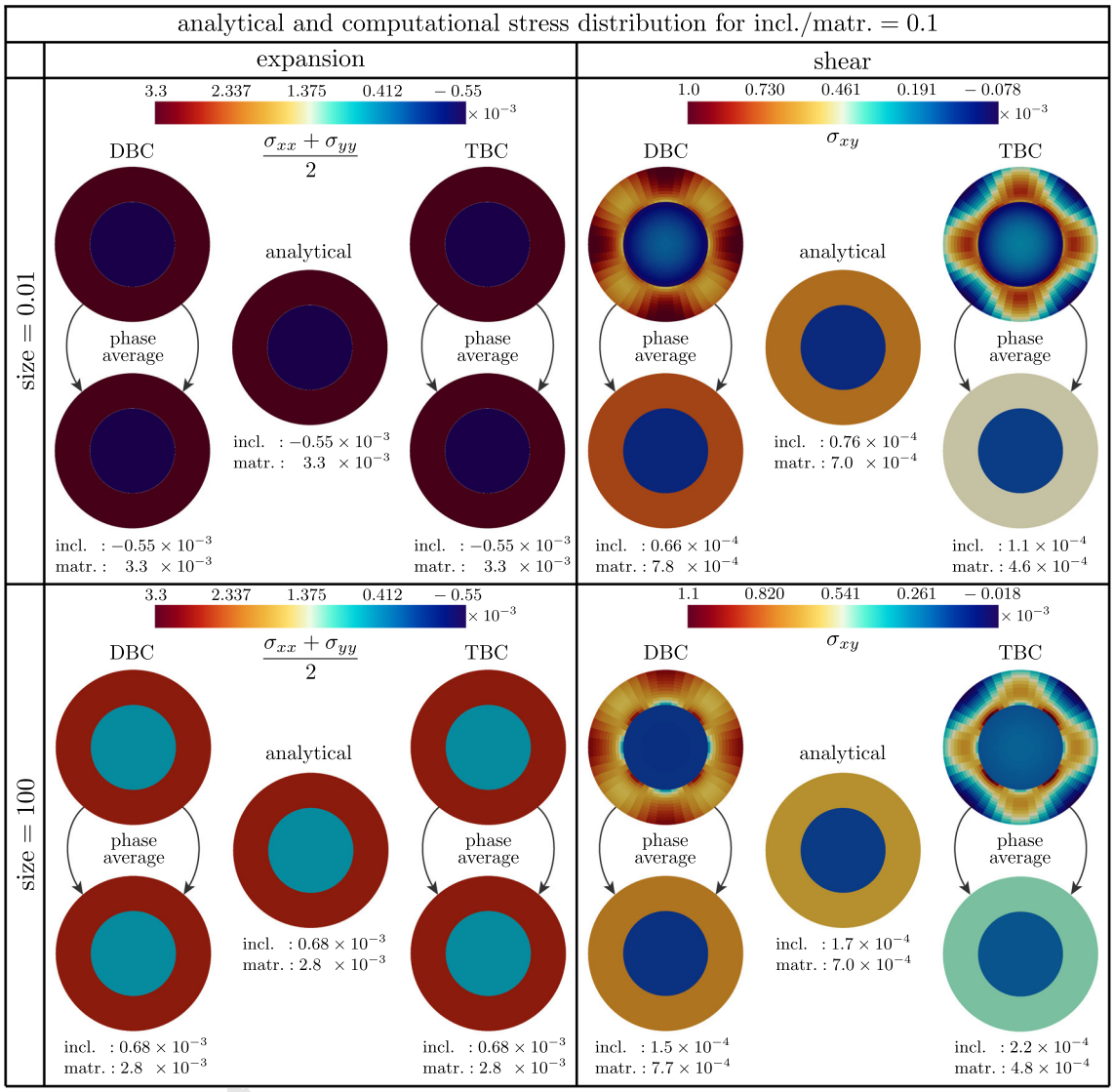

Fig. 16 Comparison of the analytical and numerical stress distributions within the RVE at different sizes for incl./matr. = 0.1. On each block, the top microstructures corresponds to the local stress distribution due to DBC and TBC. The analytical stress distribution is shown at the center. The bottom microstructures render the average of the computational stresses due to DBC and TBC

identical. Finally, when incl./matr. = 10, fiber undergoes less stress than the matrix at small sizes, whereas the opposite story holds at large sizes.

A significant feature of this contribution is that our novel formalism through the modified Mori–Tanaka approach does not only determine the overall response of composites, but also it provides information about the local fields for each phase of the medium. The purpose of the next set of examples is to evaluate the analytical stress fields and compare them against the associated numerical solutions. Figures 16, 17 and 18 provide a thorough comparison between the numerical and analytical stress distributions for different stiffness ratios at different sizes. In each figure, the rows correspond to specific sizes, whereas the columns correspond to the deformation type. Similar to Figs. 14 and 15, the stress component of the interest for the expansion and shear deformations are $[\boldsymbol{\sigma}_{xx} + \boldsymbol{\sigma}_{yy}]/2$ and $[\boldsymbol{\sigma}_{xy}]$, respectively. On each block, the top microstructures render the computational stress distribution due to DBC and TBC obtained from the finite element method. The analytical stress distribution is shown at the center of each block. Since our proposed analytical approach determines the average stress in the constituents, the bottom microstructures render the computational average stresses due to DBC and TBC suitable for comparison with analytical stresses. For the sake of clarity, the value of the average

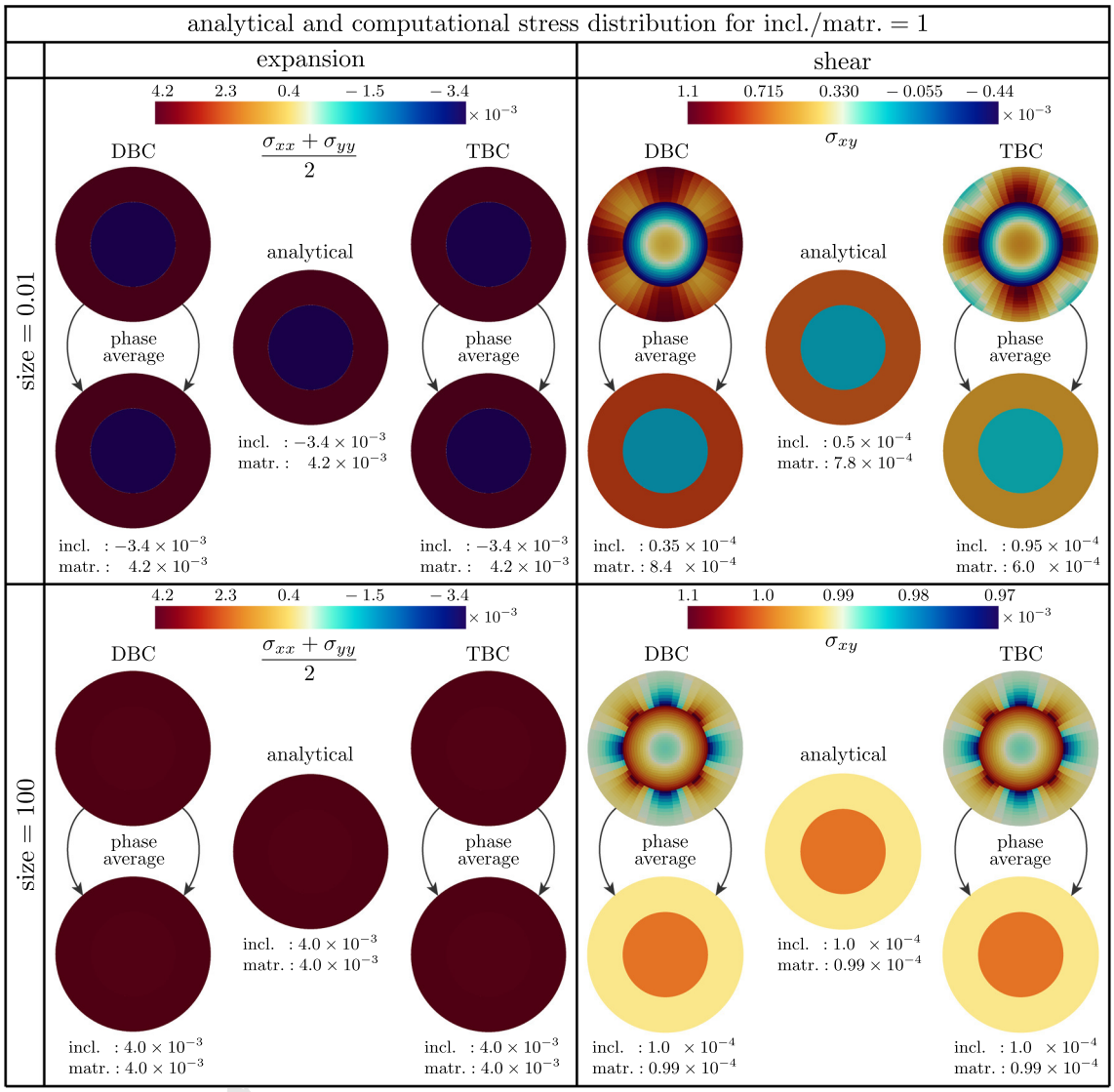

Fig. 17 Comparison of the analytical and numerical stress distributions within the RVE at different sizes for incl./matr. = 1. On each block, the top microstructures correspond to the local stress distribution due to DBC and TBC. The analytical stress distribution is shown at the center. The bottom microstructures render the average of the computational stresses due to DBC and TBC

stresses in the inclusion and the matrix is shown at the bottom of each microstructure. For the expansion case, the analytical stress is outstandingly precise and the stresses in the inclusion and matrix are exactly similar to the computational stresses. However, this is not the case for the shear deformation where various conclusions can be drawn. When incl./matr. = 0.1, the average stress due to DBC overestimates the analytical stress in the matrix. On the other hand, the average stress due to TBC underestimates the analytical stress in the matrix. For the stress in the inclusion, TBC results in the highest average stress and DBC renders the lowest average stress with the analytical stress being in between. The same story holds for incl./matr. = 1 when size is small. When size is large, both the analytical and computational stresses resemble which conforms to the coinciding bounds at large sizes in Fig. 15. For incl./matr. = 10, when size = 0.01, the stress due to DBC is the highest in the matrix and the lowest in the inclusion. TBC renders the highest inclusion average stress and lowest matrix average stress. The analytical stress in both the inclusion and the matrix are between those obtained by DBC and TBC. Finally, for incl./matr. = 10 and size = 100, both analytical and computational average stresses are similar in the matrix. However, the average stress in the inclusion is highest for DBC and the lowest for TBC with the analytical stress being in between.

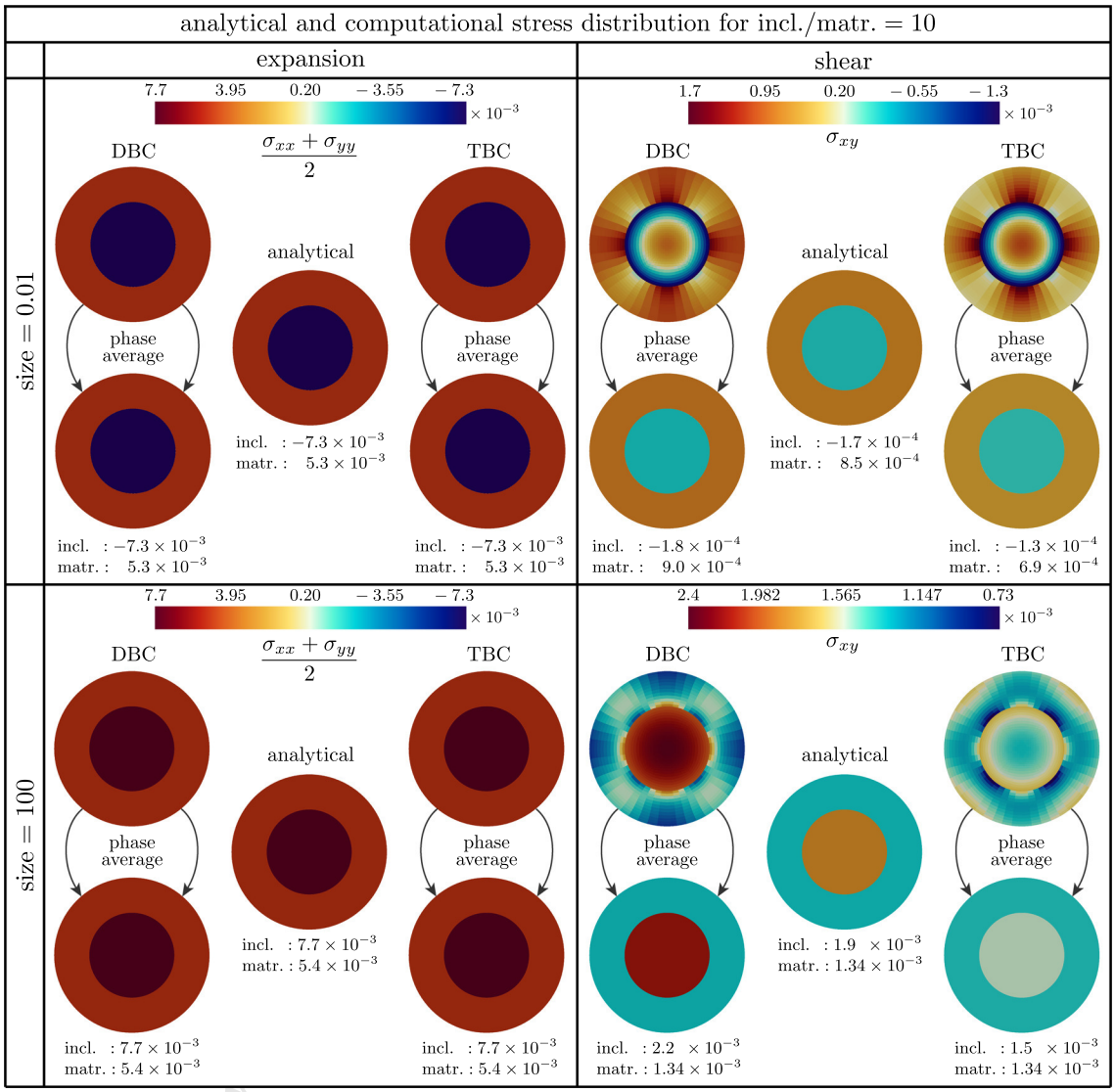

Fig. 18 Comparison of the analytical and numerical stress distributions within the RVE at different sizes for incl./matr. = 10. On each block, the top microstructures correspond to the local stress distribution due to DBC and TBC. The analytical stress distribution is shown at the center. The bottom microstructures render the average of the computational stresses due to DBC and TBC

5 Conclusion and outlook

This contribution establishes novel bounds and estimates to determine the overall behavior of composites through homogenization enhanced by general interfaces and hence the size effects. The bounds are obtained via extension of the CCA approach to account for interfaces and by prescribing displacement-type and traction-type boundary conditions on the microstructure, respectively. Our proposed strategy to compute an estimate for the effective material response, on the other hand, extends the Mori–Tanaka approach. Not only does our methodology furnish accurate results for the effective properties, but also it provides additional information about the local fields in the constituents including the interface. The proposed framework here is generic and versatile, and thus, it can readily recover perfect, cohesive and elastic interface models. Throughout a series of numerical examples, we have shown that our proposed analytical solutions are in excellent agreement with the computational results obtained from the finite element method. Furthermore, the notions of *size-dependent bounds* and *ultimate bounds* were introduced which give a crucial insight into the problem from a computational material design perspective. We believe this contribution provides a deeper understanding of the

interface effects and size-dependent behavior of continua with a variety of applications in nano-composites. Our next immediate plan is to extend the current work to 3D and study the size effects in particulate composites due to interfaces.

Appendix A: System of equations for the estimate and bounds on the shear modulus

In this section, we elaborate on the system of equations used to obtain the estimate and the bounds on the macroscopic shear modulus explained in Sect. 3.

Appendix A.1: Effective shear modulus

For this problem, the displacement fields in the matrix, fiber and the effective medium are given in Eq. (27) resulting in ten unknowns $\Xi_1^{(1)}$, $\Xi_2^{(1)}$, $\Xi_3^{(1)}$, $\Xi_4^{(1)}$, $\Xi_1^{(2)}$, $\Xi_2^{(2)}$, $\Xi_3^{(2)}$, $\Xi_4^{(2)}$, $\Xi_3^{(\mathrm{eff})}$ and $\Xi_4^{(\mathrm{eff})}$. We concluded that since the displacement at the center of the RVE must be finite, $\Xi_3^{(1)}$ and $\Xi_4^{(1)}$ must vanish. Applying the energetic criterion expressed in Eq. (30) yields $\Xi_4^{(\mathrm{eff})}$. The remaining seven unknowns are determined using the below system which is deduced from Eq. (29)

$$\boldsymbol{Q}\begin{bmatrix}\Xi_1^{(1)}\\ \Xi_2^{(1)}\\ \Xi_1^{(2)}\\ \Xi_2^{(2)}\\ \Xi_3^{(2)}\\ \Xi_4^{(2)}\end{bmatrix}=\begin{bmatrix}0\\0\\0\\0\\1\\1\end{bmatrix}+\begin{bmatrix}0\\0\\0\\0\\-\frac{3}{2}\\\frac{3}{2}\end{bmatrix}\Xi_3^{(\mathrm{eff})}, \tag{A.1}$$

with

$$\boldsymbol{Q}=\begin{bmatrix}
\frac{3\overline{\mu}\zeta_2 r_1}{\zeta_3} & \frac{\overline{\mu}}{r_1}-2\mu_1 & \frac{3\overline{\mu}\zeta_5 r_1}{\zeta_6} & \frac{\overline{\mu}}{r_1}+2\mu_2 & \frac{3\overline{\mu}}{r_1^5}+\frac{6\mu_2}{r_1^4} & -\frac{4\zeta_4}{r_1^2}-\frac{\lambda_2\overline{\mu}}{\mu_2 r_1^3}\\
-\frac{6[\overline{\mu}\zeta_2+\mu_1\zeta_1 r_1]r_1}{\zeta_3} & -\frac{2\overline{\mu}}{r_1}-2\mu_1 & -\frac{6[\overline{\mu}\zeta_5-\mu_2\zeta_4 r_1]r_1}{\zeta_6} & -\frac{2\overline{\mu}}{r_1}+2\mu_2 & -\frac{6\overline{\mu}}{r_1^5}-\frac{6\mu_2}{r_1^4} & \frac{2\zeta_4}{r_1^2}+\frac{2\overline{\mu}\lambda_2}{\mu_2 r_1^3}\\
\frac{\lambda_1 r_1^3}{\zeta_3} & \frac{\mu_1}{\overline{k}}+r_1 & -\frac{\lambda_2 r_1^3}{\zeta_6} & \frac{\mu_2}{\overline{k}}-r_1 & \frac{3\mu_2}{\overline{k}r_1^4}+\frac{1}{r_1^3} & -\frac{2\zeta_4}{\overline{k}r_1^2}-\frac{\zeta_5}{\mu_2 r_1}\\
\frac{3\mu_1\zeta_1 r_1^2}{\overline{k}\zeta_3}+r_1^3 & \frac{\mu_1}{\overline{k}}+r_1 & \frac{3\mu_2\zeta_4 r_1^2}{\overline{k}\zeta_6}-r_1^3 & \frac{\mu_2}{\overline{k}}-r_1 & -\frac{3\mu_2}{\overline{k}r_1^4}-\frac{1}{r_1^3} & \frac{\zeta_4}{\overline{k}r_1^2}-\frac{1}{r_1}\\
0 & 0 & 0 & 2\mu_2 & \frac{6\mu_2}{r_2^4} & -\frac{4\zeta_4}{r_2^2}\\
0 & 0 & \frac{6\mu_2\zeta_4 r_2^2}{\zeta_6} & 2\mu_2 & -\frac{6\mu_2}{r_2^4} & \frac{2\zeta_4}{r_2^2}
\end{bmatrix}, \tag{A.2}$$

where

$$\zeta_1 = \lambda_1 + \mu_1\,, \quad \zeta_2 = \lambda_1 + 2\mu_1\,, \quad \zeta_3 = 2\lambda_1 + 3\mu_1\,, \quad \zeta_4 = \lambda_2 + \mu_2\,, \quad \zeta_5 = \lambda_2 + 2\mu_2\,, \quad \zeta_6 = 2\lambda_2 + 3\mu_2\,.$$

Note the above system of equations is nonlinear, and thus, special treatments must be applied. We express the solution of the above system in the form

$$\begin{bmatrix} \Xi_1^{(1)} \\ \Xi_2^{(1)} \\ \Xi_1^{(2)} \\ \Xi_2^{(2)} \\ \Xi_3^{(2)} \\ \Xi_4^{(2)} \end{bmatrix} = \begin{bmatrix} g_1 \\ g_2 \\ a_1 \\ a_2 \\ a_3 \\ a_4 \end{bmatrix} + \begin{bmatrix} h_1 \\ h_2 \\ b_1 \\ b_2 \\ b_3 \\ b_4 \end{bmatrix} \Xi_3^{(\mathrm{eff})}\,. \tag{A.3}$$

The last two equations in Eq. (29) can be written as

$$a_5 + b_5\Xi_3^{(\mathrm{eff})} = \frac{c_5 + c_6\Xi_3^{(\mathrm{eff})}}{{}^{\mathrm{M}}\mu}\,, \qquad a_6 + b_6\Xi_3^{(\mathrm{eff})} = \frac{c_5 - c_6\Xi_3^{(\mathrm{eff})}}{{}^{\mathrm{M}}\mu}\,. \tag{A.4}$$

with

$$\begin{aligned}
a_5 &= \frac{\lambda_2 r_2^3}{2\lambda_2 + 3\mu_2}a_1 + r_2 a_2 - \frac{1}{r_2^3}a_3 + \frac{\lambda_2 + 2\mu_2}{\mu_2 r_2}a_4\,,\\
a_6 &= r_2^3 a_1 + r_2 a_2 + \frac{1}{r_2^3}a_3 + \frac{1}{r_2}a_4\,,\\
b_5 &= \frac{\lambda_2 r_2^3}{2\lambda_2 + 3\mu_2}b_1 + r_2 b_2 - \frac{1}{r_2^3}b_3 + \frac{\lambda_2 + 2\mu_2}{\mu_2 r_2}b_4\,,\\
b_6 &= r_2^3 b_1 + r_2 b_2 + \frac{1}{r_2^3}b_3 + \frac{1}{r_2}b_4\,,\\
c_5 &= \frac{r_2}{2}\,,\\
c_6 &= \frac{r_2}{4}\,.
\end{aligned} \tag{A.5}$$

Subtracting $(A.4)_1$ from $(A.4)_2$ gives

$$\Xi_3^{(\mathrm{eff})} = \frac{[a_5 - a_6]^{\mathrm{M}}\mu}{2c_6 + [b_6 - b_5]^{\mathrm{M}}\mu}.$$

Substituting the final result in $(A.4)_1$, after some algebra we obtain the below quadratic equation

$$[a_6 b_5 - a_5 b_6]^{\mathrm{M}}\mu^2 - [b_5 c_5 - b_6 c_5 + a_5 c_6 + a_6 c_6]^{\mathrm{M}}\mu + 2c_5 c_6 = 0\,.$$

From the two possible solutions, the positive value is the macroscopic shear modulus.

Appendix A.2: Strain bound on the shear modulus

For this problem, the displacement fields in the matrix, fiber and the effective medium are given in Eq. (32) resulting in ten unknowns $\Xi_1^{(1)}$, $\Xi_2^{(1)}$, $\Xi_3^{(1)}$, $\Xi_4^{(1)}$, $\Xi_1^{(2)}$, $\Xi_2^{(2)}$, $\Xi_3^{(2)}$ and $\Xi_4^{(2)}$. We concluded that since the

displacement at the center of the RVE must be finite, $\Xi_3^{(1)}$ and $\Xi_4^{(1)}$ must vanish. The remaining six unknowns are determined using the below system which is deduced from Eq. (33)

$$\begin{bmatrix}
\frac{3\overline{\mu}\zeta_2 r_1}{\zeta_3} & \frac{\overline{\mu}}{r_1}-2\mu_1 & \frac{3\overline{\mu}\zeta_5 r_1}{\zeta_6} & \frac{\overline{\mu}}{r_1}+2\mu_2 & \frac{3\overline{\mu}}{r_1^5}+\frac{6\mu_2}{r_1^4} & -\frac{4\zeta_4}{r_1^2}-\frac{\lambda_2\overline{\mu}}{\mu_2 r_1^3} \\
-\frac{6[\overline{\mu}\zeta_2+\mu_1\zeta_1 r_1]r_1}{\zeta_3} & -\frac{2\overline{\mu}}{r_1}-2\mu_1 & -\frac{6[\overline{\mu}\zeta_5-\mu_2\zeta_4 r_1]r_1}{\zeta_6} & -\frac{2\overline{\mu}}{r_1}+2\mu_2 & -\frac{6\overline{\mu}}{r_1^5}-\frac{6\mu_2}{r_1^4} & \frac{2\zeta_4}{r_1^2}+\frac{2\overline{\mu}\lambda_2}{\mu_2 r_1^3} \\
\frac{\lambda_1 r_1^3}{\zeta_3} & \frac{\mu_1}{\overline{k}}+r_1 & -\frac{\lambda_2 r_1^3}{\zeta_6} & \frac{\mu_2}{\overline{k}}-r_1 & \frac{3\mu_2}{\overline{k}r_1^4}+\frac{1}{r_1^3} & -\frac{2\zeta_4}{\overline{k}r_1^2}-\frac{\zeta_5}{\mu_2 r_1} \\
\frac{3\mu_1\zeta_1 r_1^2}{\overline{k}\zeta_3}+r_1^3 & \frac{\mu_1}{\overline{k}}+r_1 & \frac{3\mu_2\zeta_4 r_1^2}{\overline{k}\zeta_6}-r_1^3 & \frac{\mu_2}{\overline{k}}-r_1 & -\frac{3\mu_2}{\overline{k}r_1^4}-\frac{1}{r_1^3} & \frac{\zeta_4}{\overline{k}r_1^2}-\frac{1}{r_1} \\
0 & 0 & \frac{\lambda_2 r_2^3}{\zeta_6} & r_2 & -\frac{1}{r_2^3} & \frac{\zeta_5}{\mu_2 r_2} \\
0 & 0 & r_2^3 & r_2 & \frac{1}{r_2^3} & \frac{1}{r_2}
\end{bmatrix}
\begin{bmatrix} \Xi_1^{(1)} \\ \Xi_2^{(1)} \\ \Xi_1^{(2)} \\ \Xi_2^{(2)} \\ \Xi_3^{(2)} \\ \Xi_4^{(2)} \end{bmatrix}
=
\begin{bmatrix} 0 \\ 0 \\ 0 \\ 0 \\ r_2 \\ r_2 \end{bmatrix}, \tag{A.6}$$

where

$$\zeta_1=\lambda_1+\mu_1\,,\quad \zeta_2=\lambda_1+2\mu_1\,,\quad \zeta_3=2\lambda_1+3\mu_1\,,\quad \zeta_4=\lambda_2+\mu_2\,,\quad \zeta_5=\lambda_2+2\mu_2\,,\quad \zeta_6=2\lambda_2+3\mu_2\,.$$

Appendix A.3: Stress bound on the shear modulus

For this problem, the displacement fields in the matrix, fiber and the effective medium are given in Eq. (32) resulting in ten unknowns $\Xi_1^{(1)}$, $\Xi_2^{(1)}$, $\Xi_3^{(1)}$, $\Xi_4^{(1)}$, $\Xi_1^{(2)}$, $\Xi_2^{(2)}$, $\Xi_3^{(2)}$ and $\Xi_4^{(2)}$. We concluded that since the displacement at the center of the RVE must be finite, $\Xi_3^{(1)}$ and $\Xi_4^{(1)}$ must vanish. The remaining six unknowns are determined using the below system which is deduced from Eq. (37)

$$\begin{bmatrix}
\frac{3\overline{\mu}\zeta_2 r_1}{\zeta_3} & \frac{\overline{\mu}}{r_1}-2\mu_1 & \frac{3\overline{\mu}\zeta_5 r_1}{\zeta_6} & \frac{\overline{\mu}}{r_1}+2\mu_2 & \frac{3\overline{\mu}}{r_1^5}+\frac{6\mu_2}{r_1^4} & -\frac{4\zeta_4}{r_1^2}-\frac{\lambda_2\overline{\mu}}{\mu_2 r_1^3} \\
-\frac{6[\overline{\mu}\zeta_2+\mu_1\zeta_1 r_1]r_1}{\zeta_3} & -\frac{2\overline{\mu}}{r_1}-2\mu_1 & -\frac{6[\overline{\mu}\zeta_5-\mu_2\zeta_4 r_1]r_1}{\zeta_6} & -\frac{2\overline{\mu}}{r_1}+2\mu_2 & -\frac{6\overline{\mu}}{r_1^5}-\frac{6\mu_2}{r_1^4} & \frac{2\zeta_4}{r_1^2}+\frac{2\overline{\mu}\lambda_2}{\mu_2 r_1^3} \\
\frac{\lambda_1 r_1^3}{\zeta_3} & \frac{\mu_1}{\overline{k}}+r_1 & -\frac{\lambda_2 r_1^3}{\zeta_6} & \frac{\mu_2}{\overline{k}}-r_1 & \frac{3\mu_2}{\overline{k}r_1^4}+\frac{1}{r_1^3} & -\frac{2\zeta_4}{\overline{k}r_1^2}-\frac{\zeta_5}{\mu_2 r_1} \\
\frac{3\mu_1\zeta_1 r_1^2}{\overline{k}\zeta_3}+r_1^3 & \frac{\mu_1}{\overline{k}}+r_1 & \frac{3\mu_2\zeta_4 r_1^2}{\overline{k}\zeta_6}-r_1^3 & \frac{\mu_2}{\overline{k}}-r_1 & -\frac{3\mu_2}{\overline{k}r_1^4}-\frac{1}{r_1^3} & \frac{\zeta_4}{\overline{k}r_1^2}-\frac{1}{r_1} \\
0 & 0 & 0 & 2\mu_2 & \frac{6\mu_2}{r_2^4} & -\frac{4\zeta_4}{r_2^2} \\
0 & 0 & \frac{6\mu_2\zeta_4 r_2^2}{\zeta_6} & 2\mu_2 & -\frac{6\mu_2}{r_2^4} & \frac{2\zeta_4}{r_2^2}
\end{bmatrix}
\begin{bmatrix} \Xi_1^{(1)} \\ \Xi_2^{(1)} \\ \Xi_1^{(2)} \\ \Xi_2^{(2)} \\ \Xi_3^{(2)} \\ \Xi_4^{(2)} \end{bmatrix}
=
\begin{bmatrix} 0 \\ 0 \\ 0 \\ 0 \\ 1 \\ 1 \end{bmatrix}, \tag{A.7}$$

where

$$\zeta_1=\lambda_1+\mu_1\,,\quad \zeta_2=\lambda_1+2\mu_1\,,\quad \zeta_3=2\lambda_1+3\mu_1\,,\quad \zeta_4=\lambda_2+\mu_2\,,\quad \zeta_5=\lambda_2+2\mu_2\,,\quad \zeta_6=2\lambda_2+3\mu_2\,.$$

References

1. Javili, A.: Variational formulation of generalized interfaces for finite deformation elasticity. Math. Mech. Solids **23**, 303–322 (2017)

2. Sanchez-Palencia, E.: Comportement limite d'un probleme de transmissiona travers une plaque faiblement conductrice. Comptes Rendus Mathematique Academie des Sciences **270**, 1026–1028 (1970)
3. Pham Huy, H., Sanchez-Palencia, E.: Phénomènes de transmission à travers des couches minces de conductivitéélevée. J. Math. Anal. Appl. **47**, 284–309 (1974)
4. Hashin, Z.: Thin interphase/imperfect interface in conduction. J. Appl. Phys. **89**, 2261–2267 (2001)
5. Hill, R.: Elastic properties of reinforced solids: some theoretical principles. J. Mech. Phys. Solids **11**, 357–372 (1963)
6. Hill, R.: On constitutive macro-variables for heterogeneous solids at finite strain. Proc. R. Soc. A **326**, 131–147 (1972)
7. Ogden, R.W.: On the overall moduli of non-linear elastic composite materials. J. Mech. Phys. Solids **22**, 541–553 (1974)
8. Gurtin, M.E., Murdoch, A.I.: A continuum theory of elastic material surfaces. Arch. Ration. Mech. Anal. **57**, 291–323 (1975)
9. Moeckel, G.P.: Thermodynamics of an interface. Arch. Ration. Mech. Anal. **57**, 255–280 (1975)
10. Murdoch, A.I.: A thermodynamical theory of elastic material interfaces. Q. J. Mech. Appl. Math. **29**, 245–275 (1976)
11. Daher, N., Maugin, G.A.: The method of virtual power in continuum mechanics application to media presenting singular surfaces and interfaces. Acta Mechanica **60**, 217–240 (1986)
12. dell'Isola, F., Romano, A.: On the derivation of thermomechanical balance equations for continuous system with a nonmaterial interface. Int. J. Eng. Sci. **25**, 1459–1468 (1987)
13. Fried, E., Gurtin, M.E.: Thermomechanics of the interface between a body and its environment. Contin. Mech. Thermodyn. **19**, 253–271 (2007)
14. Klarbring, A.: Derivation of a model of adhesively bonded joints by the asymptotic expansion method. Int. J. Eng. Sci. **29**, 493–512 (1991)
15. Klarbring, A., Movchan, A.B.: Asymptotic modelling of adhesive joints. Mech. Mater. **28**, 137–145 (1998)
16. Chen, T., Chiu, M.S., Weng, C.N.: Derivation of the generalized Young-Laplace equation of curved interfaces in nanoscaled solids. J. Appl. Phys. **100**, 074308 (2006)
17. Javili, A., McBride, A., Steinmann, P.: Thermomechanics of solids with lower-dimensional energetics: on the importance of surface, interface, and curve structures at the nanoscale. A unifying review. Appl. Mech. Rev. **65**, 010802 (2013a)
18. Javili, A.: A note on traction continuity across an interface in a geometrically non-linear framework. Math. Mech. Solids. https://doi.org/10.1177/1081286518766980
19. Huang, Z.P., Sun, L.: Size-dependent effective properties of a heterogeneous material with interface energy effect: from finite deformation theory to infinitesimal strain analysis. Acta Mechanica **190**, 151–163 (2007)
20. Huang, Z.P., Wang, J.: A theory of hyperelasticity of multi-phase media with surface/interface energy effect. Acta Mechanica **182**, 195–210 (2006)
21. Altenbach, H., Eremeyev, V.A.: On the shell theory on the nanoscale with surface stresses. Int. J. Eng. Sci. **49**, 1294–1301 (2011)
22. Chhapadia, P., Mohammadi, P., Sharma, P.: Curvature-dependent surface energy and implications for nanostructures. J. Mech. Phys. Solids **59**, 2103–2115 (2011)
23. Cordero, N.M., Forest, S., Busso, E.P.: Second strain gradient elasticity of nano-objects. J. Mech. Phys. Solids **97**, 92–124 (2016)
24. Dingreville, R., Hallil, A., Berbenni, S.: From coherent to incoherent mismatched interfaces: a generalized continuum formulation of surface stresses. J. Mech. Phys. Solids **72**, 40–60 (2014)
25. Dingreville, R., Qu, J.: Interfacial excess energy, excess stress and excess strain in elastic solids: Planar interfaces. J. Mech. Phys. Solids **56**, 1944–1954 (2008)
26. Duan, H.L., Wang, J., Karihaloo, B.L.: Theory of elasticity at the nanoscale. Adv. Appl. Mech. **42**, 1–68 (2009)
27. Fried, E., Todres, R.E.: Mind the gap: the shape of the free surface of a rubber-like material in proximity to a rigid contactor. J. Elast. **80**, 97–151 (2005)
28. Gurtin, M.E., Weissmüller, J., Larché, F.: A general theory of curved deformable interfaces in solids at equilibrium. Philos. Mag. A **78**, 1093–1109 (1998)
29. Javili, A., Mcbride, A., Mergheim, J., Steinmann, P., Schmidt, U.: Micro-to-macro transitions for continua with surface structure at the microscale. Int. J. Solids Struct. **50**, 2561–2572 (2013b)
30. Liu, L., Yu, M., Lin, H., Foty, R.: Deformation and relaxation of an incompressible viscoelastic body with surface viscoelasticity. J. Mech. Phys. Solids **98**, 309–329 (2017)
31. Steigmann, D.J., Ogden, R.W.: Elastic surface–substrate interactions. Proc. R. Soc. Lond. A **455**, 437–474 (1999)
32. Wang, Z.Q., Zhao, Y.P., Huang, Z.P.: The effects of surface tension on the elastic properties of nano structures. Int. J. Eng. Sci. **48**, 140–150 (2010)
33. Zhong, Z., Meguid, S.A.: On the elastic field of a spherical inhomogeneity with an imperfectly bonded interface. J. Elast. **46**, 91–113 (1997)
34. Han, Z., Mogilevskaya, S.G., Schillinger, D.: Local fields and overall transverse properties of unidirectional composite materials with multiple nanofibers and SteigmannOgden interfaces. Int. J. Solids Struct. **147**, 166–182 (2018)
35. Fedotov, A.: Interface model of homogenization for analysing the influence of inclusion size on the elastic properties of composites. Compos. B Eng. **152**, 241–247 (2018)
36. Barenblatt, G.I.: The formation of equilibrium cracks during brittle fracture. General ideas and hypotheses. Axially-symmetric cracks. J. Appl. Math. Mech. **23**, 622–636 (1959)
37. Barenblatt, G.I.: The mathematical theory of equilibrium of crack in brittle fracture. Adv. Appl. Mech. **7**, 55–129 (1962)
38. Dugdale, D.S.: Yielding of steel sheets containing slits. J. Mech. Phys. Solids **8**, 100–104 (1960)
39. Needleman, A.: A continuum model for void nucleation by inclusion debonding. J. Appl. Mech. **54**, 525–531 (1987)
40. van den Bosch, M.J., Schreurs, P.J.G., Geers, M.G.D.: An improved description of the exponential Xu and Needleman cohesive zone law for mixed-mode decohesion. Eng. Fract. Mech. **73**, 1220–1234 (2006)
41. Wells, G.N., Sluys, L.J.: A new method for modelling cohesive cracks using finite elements. Int. J. Numer. Methods Eng. **50**, 2667–2682 (2001)

42. Remmers, J.J.C., de Borst, R., Needleman, A.: The simulation of dynamic crack propagation using the cohesive segments method. J. Mech. Phys. Solids **56**, 70–92 (2008)
43. Moës, N., Belytschko, T.: Extended finite element method for cohesive crack growth. Eng. Fract. Mech. **69**, 813–833 (2002)
44. Alfano, G., Crisfield, M.A.: Finite element interface models for the delamination analysis of laminated composites: mechanical and computational issues. Int. J. Numer. Methods Eng. **50**, 1701–1736 (2001)
45. Charlotte, M., Laverne, J., Marigo, J.J.: Initiation of cracks with cohesive force models: a variational approach. Eur. J. Mech. A/Solids **25**, 649–669 (2006)
46. Despringre, N., Chemisky, Y., Bonnay, K., Meraghni, F.: Micromechanical modeling of damage and load transfer in particulate composites with partially debonded interface. Compos. Struct. **155**, 77–88 (2016)
47. Dimitri, R., Trullo, M., De Lorenzis, L., Zavarise, G.: Coupled cohesive zone models for mixed-mode fracture: a comparative study. Eng. Fract. Mech. **148**, 145–179 (2015)
48. Fagerström, M., Larsson, R.: Theory and numerics for finite deformation fracture modelling using strong discontinuities. Int. J. Numer. Methods Eng. **66**, 911–948 (2006)
49. Gasser, T.C., Holzapfel, G.A.: Geometrically non-linear and consistently linearized embedded strong discontinuity models for 3D problems with an application to the dissection analysis of soft biological tissues. Comput. Methods Appl. Mech. Eng. **192**, 5059–5098 (2003)
50. Ortiz, M., Pandolfi, A.: Finite-deformation irreversible cohesive elements for three-dimensional crack-propagation analysis. Int. J. Numer. Methods Eng. **1282**, 1267–1282 (1999)
51. Park, K., Paulino, G.H.: Cohesive zone models: a critical review of traction-separation relationships across fracture surfaces. Appl. Mech. Rev. **64**, 060802 (2011)
52. Park, K., Paulino, G.H., Roesler, J.R.: A unified potential-based cohesive model of mixed-mode fracture. J. Mech. Phys. Solids **57**, 891–908 (2009)
53. Tijssens, M.G.A., Sluys, B.L.J., Van der Giessen, E.: Numerical simulation of quasi-brittle fracture using damaging cohesive surfaces. Eur. J. Mech. A/Solids **19**, 761–779 (2000)
54. Wu, C., Gowrishankar, S., Huang, R., Liechti, K.M.: On determining mixed-mode traction–separation relations for interfaces. Int. J. Fract. **202**, 1–19 (2016)
55. Qian, J., Lin, J., Xu, G.K., Lin, Y., Gao, H.: Thermally assisted peeling of an elastic strip in adhesion with a substrate via molecular bonds. J. Mech. Phys. Solids **101**, 197–208 (2017)
56. Wang, J., Duan, H.L., Zhang, Z., Huang, Z.P.: An anti-interpenetration model and connections between interphase and interface models in particle-reinforced composites. Int. J. Mech. Sci. **47**, 701–718 (2005)
57. Mosler, J., Scheider, I.: A thermodynamically and variationally consistent class of damage-type cohesive models. J. Mech. Phys. Solids **59**, 1647–1668 (2011)
58. Hashin, Z.: Thin interphase/imperfect interface in elasticity with application to coated fiber composites. J. Mech. Phys. Solids **50**, 2509–2537 (2002)
59. Benveniste, Y.: A general interface model for a three-dimensional curved thin anisotropic interphase between two anisotropic media. J. Mech. Phys. Solids **54**, 708–734 (2006)
60. Benveniste, Y.: Models of thin interphases with variable moduli in plane-strain elasticity. Math. Mech. Solids **18**, 119–134 (2013)
61. Benveniste, Y., Miloh, T.: Imperfect soft and stiff interfaces in two-dimensional elasticity. Mech. Mater. **33**, 309–323 (2001)
62. Gu, S.T., He, Q.C.: Interfacial discontinuity relations for coupled multifield phenomena and their application to the modeling of thin interphases as imperfect interfaces. J. Mech. Phys. Solids **59**, 1413–1426 (2011)
63. Gu, S.T., Monteiro, E., He, Q.C.: Coordinate-free derivation and weak formulation of a general imperfect interface model for thermal conduction in composites. Compos. Sci. Technol. **71**, 1209–1216 (2011)
64. Monchiet, V., Bonnet, G.: Interfacial models in viscoplastic composites materials. Int. J. Eng. Sci. **48**, 1762–1768 (2010)
65. Chatzigeorgiou, G., Meraghni, F., Javili, A.: Generalized interfacial energy and size effects in composites. J. Mech. Phys. Solids **106**, 257–282 (2017)
66. Gu, S.T., Liu, J.T., He, Q.C.: Size-dependent effective elastic moduli of particulate composites with interfacial displacement and traction discontinuities. Int. J. Solids Struct. **51**, 2283–2296 (2014)
67. Koutsawa, Y., Karatrantos, A., Yu, W., Ruch, D.: A micromechanics approach for the effective thermal conductivity of composite materials with general linear imperfect interfaces. Compos. Struct. **200**, 747–756 (2018)
68. Firooz, S., Javili, A.: Understanding the role of general interfaces in the overall behavior of composites and size effects. Comput. Mater. Sci. **162**, 245–254 (2019)
69. Brisard, S., Dormieux, L., Kondo, D.: Hashin–Shtrikman bounds on the shear modulus of a nanocomposite with spherical inclusions and interface effects. Comput. Mater. Sci. **50**, 403–410 (2010)
70. Chatzigeorgiou, G., Javili, A., Steinmann, P.: Multiscale modelling for composites with energetic interfaces at the micro- or nanoscale. Math. Mech. Solids **20**, 1130–1145 (2015)
71. Duan, H.L., Karihaloo, B.L.: Effective thermal conductivities of heterogeneous media containing multiple imperfectly bonded inclusions. Phys. Rev. B **75**, 064206 (2007)
72. Duan, H.L., Wang, J., Huang, Z.P., Karihaloo, B.L.: Size-dependent effective elastic constants of solids containing nano-inhomogeneities with interface stress. J. Mech. Phys. Solids **53**, 1574–1596 (2005)
73. Lim, C.W., Li, Z.R., He, L.H.: Size dependent, non-uniform elastic field inside a nano-scale spherical inclusion due to interface stress. Int. J. Solids Struct. **43**, 5055–5065 (2006)
74. Mogilevskaya, S.G., Crouch, S.L., Stolarski, H.K.: Multiple interacting circular nano-inhomogeneities with surface/interface effects. J. Mech. Phys. Solids **56**, 2298–2327 (2008)
75. Nazarenko, L., Bargmann, S., Stolarski, H.: Closed-form formulas for the effective properties of random particulate nanocomposites with complete Gurtin–Murdoch model of material surfaces. Contin. Mech. Thermodyn. **29**, 77–96 (2017)
76. Sharma, P.: Size-dependent elastic fields of embedded inclusions in isotropic chiral solids. Int. J. Solids Struct. **41**, 6317–6333 (2004)

77. Sharma, P., Ganti, S., Bhate, N.: Effect of surfaces on the size-dependent elastic state of nano-inhomogeneities. Appl. Phys. Lett. **82**, 535–537 (2003)
78. Sharma, P., Wheeler, L.T.: Size-dependent elastic state of ellipsoidal nano-inclusions incorporating surface/interface tension. J. Appl. Mech. **74**, 447–454 (2007)
79. Tian, L., Rajapakse, R.K.N.D.: Analytical solution for size-dependent elastic field of a nanoscale circular inhomogeneity. J. Appl. Mech. **74**, 568–574 (2007)
80. Fritzen, F., Leuschner, M.: Nonlinear reduced order homogenization of materials including cohesive interfaces. Comput. Mech. **56**, 131–151 (2015)
81. Javili, A., dell'Isola, F., Steinmann, P.: Geometrically nonlinear higher-gradient elasticity with energetic boundaries. J. Mech. Phys. Solids **61**, 2381–2401 (2013c)
82. Monteiro, E., He, Q.C., Yvonnet, J.: Hyperelastic large deformations of two-phase composites with membrane-type interface. Int. J. Eng. Sci. **49**, 985–1000 (2011)
83. Tu, W., Pindera, M.J.: Cohesive zone-based damage evolution in periodic materials via finite-volume homogenization. J. Appl. Mech. **81**, 101005 (2014)
84. Yvonnet, J., Quang, H.L., He, Q.C.: An XFEM/level set approach to modelling surface/interface effects and to computing the size-dependent effective properties of nanocomposites. Comput. Mech. **42**, 119–131 (2008)
85. Davydov, D., Javili, A., Steinmann, P.: On molecular statics and surface-enhanced continuum modeling of nano-structures. Comput. Mater. Sci. **69**, 510–519 (2013)
86. Elsner, B.A.M., Müller, S., Bargmann, S., Weissmüller, J.: Surface excess elasticity of gold: Ab initio coefficients and impact on the effective elastic response of nanowires. Acta Materialia **124**, 468–477 (2017)
87. He, J., Lilley, C.M.: Surface effect on the elastic behavior of static bending nanowires. Nano Lett. **8**, 1798–1802 (2008)
88. Levitas, V.I., Samani, K.: Size and mechanics effects in surface-induced melting of nanoparticles. Nature Commun. **2**, 284–286 (2011)
89. Olsson, P.A.T., Park, H.S.: On the importance of surface elastic contributions to the flexural rigidity of nanowires. J. Mech. Phys. Solids **60**, 2064–2083 (2012)
90. Park, H.S., Klein, P.A.: Surface stress effects on the resonant properties of metal nanowires: the importance of finite deformation kinematics and the impact of the residual surface stress. J. Mech. Phys. Solids **56**, 3144–3166 (2008)
91. Javili, A., Steinmann, P., Mosler, J.: Micro-to-macro transition accounting for general imperfect interfaces. Comput. Methods Appl. Mech. Eng. **317**, 274–317 (2017)
92. McBride, A., Mergheim, J., Javili, A., Steinmann, P., Bargmann, S.: Micro-to-macro transitions for heterogeneous material layers accounting for in-plane stretch. J. Mech. Phys. Solids **60**, 1221–1239 (2012)
93. Saeb, S., Steinmann, P., Javili, A.: Aspects of computational homogenization at finite deformations: a unifying review from Reuss' to Voigt's Bound. Appl. Mech. Rev. **68**, 050801 (2016)
94. Kanouté, P., Boso, D.P., Chaboche, J.L., Schrefler, B.A.: Multiscale methods for composites: a review. Arch. Comput. Methods Eng. **16**, 31–75 (2009)
95. Charalambakis, N., Chatzigeorgiou, G., Chemisky, Y., Meraghni, F.: Mathematical homogenization of inelastic dissipative materials: a survey and recent progress. Contin. Mech. Thermodyn. **30**, 1–51 (2018)
96. Matouš, K., Geers, M.G.D., Kouznetsova, V.G., Gillman, A.: A review of predictive nonlinear theories for multiscale modeling of heterogeneous materials. J. Comput. Phys. **330**, 192–220 (2017)
97. Chen, Q., Wang, G., Pindera, M.J.: Homogenization and localization of nanoporous composites—A critical review and new developments. Compos. B Eng. **155**, 329–368 (2018)
98. Pindera, M.J., Khatam, H., Drago, A.S., Bansal, Y.: Micromechanics of spatially uniform heterogeneous media: a critical review and emerging approaches. Compos. B Eng. **40**, 349–378 (2009)
99. Khisaeva, Z.F., Ostoja-Starzewski, M.: On the size of RVE in finite elasticity of random composites. J. Elast. **85**, 153–173 (2006)
100. Temizer, I., Zohdi, T.I.: A numerical method for homogenization in non-linear elasticity. Comput. Mech. **40**, 281–298 (2007)
101. Gitman, I.M., Askes, H., Aifantis, E.C.: The representative volume size in static and dynamic micro-macro transitions. Int. J. Fract. **135**, 3–9 (2005)
102. Kanit, T., Forest, S., Galliet, I., Mounoury, V., Jeulin, D.: Determination of the size of the representative volume element for random composites: statistical and numerical approach. Int. J. Solids Struct. **40**, 3647–3679 (2003)
103. Firooz, S., Saeb, S., Chatzigeorgiou, G., Meraghni, F., Steinmann, P., Javili, A.: Systematic study of homogenization and the utility of circular simplified representative volume element. Math. Mech. Solids. https://doi.org/10.1177/1081286518823834
104. Chatzigeorgiou, G., Seidel, G.D., Lagoudas, D.C.: Effective mechanical properties of "fuzzy fiber" composites. Compos. B **43**, 2577–2593 (2012)
105. Dinzart, F., Sabar, H.: New micromechanical modeling of the elastic behavior of composite materials with ellipsoidal reinforcements and imperfect interfaces. Int. J. Solids Struct. **108**, 254–262 (2017)
106. Christensen, R.M., Lo, K.H.: Solutions for effective shear properties in three phase sphere and cylinder models. J. Mech. Phys. Solids **27**, 315–330 (1979)
107. Hashin, Z., Rosen, B.W.: The elastic moduli of fiber-reinforced materials. J. Appl. Mech. **31**, 223–232 (1964)
108. Duan, H.L., Yi, X., Huang, Z.P., Wang, J.: A unified scheme for prediction of effective moduli of multiphase composites with interface effects. Part I: Theoretical framework. Mech. Mater. **39**, 81–93 (2007)
109. Eshelby, J.D.: The determination of the elastic field of an ellipsoidal inclusion, and related problems. Proc. R. Soc. A **241**, 376–396 (1957)
110. Benveniste, Y., Dvorak, G.J., Chen, T.: Stress fields in composites with coated inclusions. Mech. Mater. **7**, 305–317 (1989)
111. Wang, Z., Oelkers, R.J., Lee, K.C., Fisher, F.T.: Annular coated inclusion model and applications for polymer nanocomposites-Part I: Spherical inclusions. Mech. Mater. **101**, 170–184 (2016a)

805 112. Wang, Z., Oelkers, R.J., Lee, K.C., Fisher, F.T.: Annular coated inclusion model and applications for polymer
806 nanocomposites-Part II: Cylindrical inclusions. Mech. Mater. **101**, 50–60 (2016b)
807 113. Benveniste, Y., Dvorak, G.J., Chen, T.: On diagonal and elastic symmetry of the approximate effective stiffness tensor of
808 heterogeneous media. J. Mech. Phys. Solids **39**(7), 927–946 (1991)
809 114. Hashin, Z.: Thermoelastic properties of fiber composites with imperfect interface. Mech. Mater. **8**, 333–348 (1990)

Journal: 161
Article:

Author Query Form

Please ensure you fill out your response to the queries raised below and return this form along with your corrections

Dear Author

During the process of typesetting your article, the following queries have arisen. Please check your typeset proof carefully against the queries listed below and mark the necessary changes either directly on the proof/online grid or in the 'Author's response' area provided below

Query	Details required	Author's response
1.	Please check that the terms 'micro-structure' and 'micro-scale' have been changed to 'microstructure' and 'microscale', respectively, in the article.	